THE SPECTRAL ENERGY DISTRIBUTION AND MASS-LOSS RATE OF THE A-TYPE SUPERGIANT DENEB

J. P. Aufdenberg

Solar and Stellar Physics Division, Harvard-Smithsonian Center for Astrophysics, 60 Garden Street, Mail Stop 15, Cambridge, MA 02138
jaufdenberg@cfa.harvard.edu

P. H. Hauschildt

Department of Physics and Astronomy & Center for Simulational Physics, University of Georgia, Athens, GA 30602-2451
yeti@hal.physast.uga.edu

E. Baron

Department of Physics and Astronomy, University of Oklahoma, Norman, OK 73019-0260
baron@nhn.ou.edu

T. E. Nordgren

Department of Physics, University of Redlands, 1200 East Colton Ave, Redlands, CA 92373
tyler_nordgren@redlands.edu

I. D. Howarth, A. W. Burnley

Department of Physics and Astronomy, University College London, Gower Street, London WC1E 6BT, UK
idh@star.ucl.ac.uk, awxb@star.ucl.ac.uk

and

K. D. Gordon, J. A. Stansberry

Steward Observatory, 933 N Cherry Ave, University of Arizona, Tucson, AZ 85721
kgordon@as.arizona.edu,stansber@as.arizona.edu

Draft version February 1, 2008

ABSTRACT

A stellar wind module has been developed for the `PHOENIX` stellar atmosphere code for the purpose of computing non-LTE, line-blanketed, expanding atmospheric structures and detailed synthetic spectra of hot luminous stars with winds. We apply the code to observations of Deneb, for which we report the first positive detections of mm and cm emission (obtained using the SCUBA and the VLA), as well a strong upper limit on the 850μm flux (using the HHT). The slope of the radio spectrum shows that the stellar wind is partially ionized. We report a uniform-disk angular diameter measurement, $\overline{\theta_{\rm UD}} = 2.40 \pm 0.06$ mas, from the Navy Prototype Optical Interferometer (NPOI). The measured bolometric flux and corrected NPOI angular diameter yield an effective temperature of 8600 ± 500 K. Least-squares comparisons of synthetic spectral energy distributions from 1220 Å to 3.6 cm with the observations provide estimates for the effective temperature and the mass-loss rate of $\simeq 8400 \pm 100$ K and $8 \pm 3 \times 10^{-7}$ $M_\odot$ yr^{-1}, respectively. This range of mass-loss rates is consistent with that derived from high dispersion UV spectra when non-LTE metal-line blanketing is considered. We are unable achieve a reasonable fit to a typical Hα P-Cygni profile with any model parameters over a reasonable range. This is troubling because the Hα profile is the observational basis for Wind Momentum-Luminosity Relationship.

Subject headings: methods: numerical — radio continuum: stars — stars: atmospheres — stars:individual (Deneb) — stars: winds, outflows — techniques: interferometric

1. INTRODUCTION

A-type supergiants are the brightest stars at visual wavelengths (up to $M_V \simeq -9$) and are therefore among the brightest single stars visible in galaxies. For this reason, these stars have been of increasing interest in extragalactic astronomy where they show potential as independent distance indicators (Bresolin et al. 2001; Kudritzki et al. 1999, hereafter K99). This potential lies in the use of the Wind Momentum-Luminosity Relationship (WMLR) which is derived from Sobolev radiation-driven stellar wind theory (K99 and references therein). Testing this relationship and the theory of radiation driven winds most critically requires an accurate determination of the stellar mass-loss rates. The WMLR states that $\dot{M}v_\infty \propto L^{1/\alpha}/R_\star^{0.5}$, where $\dot{M}$ is the mass-loss rate, v_∞ is the terminal velocity of the wind, $R_\star$ is a photospheric reference radius, and α is a parameter related to the distribution of atomic line strengths for the spectral lines which drive the wind.

The application of the WMLR to nearby galaxies requires a calibration of the relationship using similar stars in the Milky Way. To determine mass-loss rates for A-type supergiants, K99 modeled the hydrogen Balmer lines Hα and Hγ for six stars in the Galaxy and M31 using a unified stellar atmosphere model. In their analysis, K99 synthesized the observed line profiles by adjusting model values for the mass-loss rate, the velocity law exponent β, and a line-broadening parameter, v_t, after first adopting parameters for the effective temperature, $T_{\rm eff}$, the radius, $R_\star$, the gravity, $\log g$, and the projected stellar rotational velocity.

The use of the Hα profile as the sole diagnostic of A-type supergiant wind momenta is problematic because Hα emission observed in stars of this type is known to be strongly variable (Rosendhal 1972; Kaufer et al. 1996). Nevertheless, the accuracy of mass-loss rate determinations for A-type supergiants in M31 is claimed to be at the level of 15% (McCarthy et al. 1997). However, there has been no consensus on the mass-loss rate for Deneb (α Cyg, HD 197345, spectral type A2Ia according to Morgan & Keenan (1973)), the brighest, nearest, and best-studied A-type supergiant, which we might expect to serve as an archetype and benchmark. Published estimates of its mass-loss rate range over more than three orders of magnitude, from methods which include modeling the line profiles Mg II $\lambda2802$ (Kunasz & Praderie 1981, $3.1 \times 10^{-9} - 1.5 \times 10^{-7}$ M$_\odot$ yr^{-1}) and Hα (Kunasz & Morrison 1982; Scuderi et al. 1992, $1.7 \pm 0.4 \times 10^{-7}$ M$_\odot$ yr^{-1}; $3.7 \pm 0.8 \times 10^{-6}$ M$_\odot$ yr^{-1}), analysing low-excitation Fe II lines in the ultraviolet (Hensberge et al. 1982, $1 - 5 \times 10^{-9}$ M$_\odot$ yr^{-1}), modeling the IR excess (Barlow & Cohen 1977, 6×10^{-7} M$_\odot$ yr^{-1}), and radio-flux limits (Abbott et al. 1984, $\leq 2 \times 10^{-7}$ M$_\odot$ yr^{-1}).

It is not unreasonable to suggest that the degree to which we understand A-type supergiants in general may be tested by Deneb. Therefore, it is troubling that the published mass-loss estimates for Deneb vary so widely and this fact casts doubt on the what we can infer about the properties of more distant A-type supergiants. The proximity of Deneb allows one to more rigorously constrain its physical parameters and apply several different techniques to estimate its mass-loss rate.

For these reasons, in this paper we investiage Deneb's fundamental properties, and in particular its mass-loss rate. To do this we employ a new stellar wind-model atmosphere package developed by Aufdenberg (2000) for use with the PHOENIX[1] general-purpose stellar and planetary atmosphere code (Hauschildt & Baron 1999, and references therein) and bring together new observations of Deneb at visible, infrared, millimeter, and radio wavelengths.

Our principal motivation for the constructing unified wind models has been that most analyses of early-type supergiants still suffer from severe limitations present in the model atmospheres which are employed. Recent systematic analyses (Verdugo et al. 1999) of the atmospheric parameters of A-type supergiants have employed LTE, line-blanketed, plane-parallel, static model atmospheres. These models do not include the effects (on the temperature structure and the synthetic spectrum) of metal line-blanketing and a spherically extended expanding atmosphere. Furthermore, most analyses do not allow for departures from LTE, particularly for species heavier than H and He, in computation of the opacity and line formation, which are especially important in low-density extended atmospheres. Santolaya-Rey et al. (1997) have developed models, employed by K99, which address many of these limitations including the solution of the spherical expanding transfer equation in the co-moving frame and the non-LTE treatment of hydrogen and helium. Despite these important improvements, these models have had limited success in fitting spectral energy distributions (SEDs) due to the lack of metal line-blanketing in both the atmospheric structure and the synthetic spectrum. Fundamental stellar parameters derived from line-profile fitting of hydrogen and helium lines alone may not be consistent with the SED. Therefore, we believe that fitting both the line spectrum and the SED simultaneously should lead to more robust atmospheric parameters for A-type supergiants.

In §2 we describe the spectrophotometric, spectroscopic, and interferometric observations used here. In §3 limb-darkening models and corrections to the angular diamter are discussed. The effective temperature, reddening and other parameters constrained by the observations are discussed in §4. In §5 we compare the spectrophotometic data from the UV to the radio with our synthetic spectral energy distributions. The comparison of our models to portions of Deneb's line spectrum is discussed in §6. We summarize our results and conclusions in §7. Details on the model atmosphere construction and computation are left for Appendix A.

2. OBSERVATIONS

Previous radio observations of Deneb (Drake & Linsky 1989, and references therein) have yielded only upper limits. We report positive detections of radiation from Deneb at 1.35 mm with the Submillimetre Common-User Bolometer Array (SCUBA) located on the James Clerk Maxwell Telescope (JCMT) and at 3.6 cm with the Very Large Array (VLA). In addition, two of us (KDG & JAS) observed Deneb at 870 μm with the Heinrich Hertz Telescope (HHT) and we report an upper limit on the flux density at this wavelength. Futhermore, one of us (TEN) measured Deneb's angular diameter, previously uncertain at the 30% level, with the Navy Prototype Optical Interferometer (NPOI) and we present an angular diameter measurement accurate to 3%. In addition to these new data, we have brought together observations of Deneb from Infrared Processing and Analysis Center (IPAC) data archive. The IR, millimeter and radio data are summarized in Table 1.

2.1. SCUBA Observation

SCUBA was used to observe Deneb on 4 May 1998. Four runs were made in the photometery mode using the 1350 μm filter. Each run consisted of 50 integrations of 18 sec each. Each integration includes both the on-source and off-source time, the on-source time is half the value. Deneb was positively detected at 1.35 mm with flux density of 7.8$\pm$ 1.9 mJy.

2.2. VLA Observation

Deneb was observed by 22 antennas of the VLA in the D$\longrightarrow$A array configuration on 29 January 1990. The central frequency of the observation was 8414 MHz with bandwidth of 50 MHz. The total observation time was 4800 sec, with 3450 sec on source. Deneb was positively detected at 3.6 cm with a flux density of 0.23$\pm$0.05 mJy.

---

[1] Also see http://phoenix.physast.uga.edu

Table 1

Infrared, Millimeter, and Radio Photometry of Deneb

Wavelength	Flux Density	Observation
1.25 μm	609 ± 19 Jy	COBE/DIRBE band 1A [a]
2.2 μm	268 ± 8 Jy	COBE/DIRBE band 2A [a]
2.2 μm	282 ± 28 Jy	IRTF K band [b]
3.5 μm	125 ± 4 Jy	COBE/DIRBE band 3A [a]
3.5 μm	122 ± 12 Jy	IRTF L band [b]
4.29 μm	89.5 ± 9.5 Jy	MSX band B1 [c]
4.35 μm	84.5 ± 8.0 Jy	MSX band B2 [c]
4.8 μm	81 ± 8 Jy	IRTF M band [b]
4.9 μm	74.5 ± 2.2 Jy	COBE/DIRBE band 4 [a]
7.76 μm	33.6 ± 1.7 Jy	MSX band A [c]
10.2 μm	22 ± 2 Jy	IRTF N band [b]
11.99 μm	15.6 ± 0.5 Jy	MSX band B [c]
14.55 μm	11.2 ± 0.5 Jy	MSX band C [c]
20.0 μm	6.7 ± 0.7 Jy	IRTF Q band [b]
20.68 μm	5.38 ± 0.45 Jy	MSX band D [c]
60 μm	957 ± 287 mJy	ISOPHOT [d]
870 μm	< 24 mJy	HHT [d]
1.35 mm	7.8 ± 1.9 mJy	SCUBA [d]
2 cm	< 1.0 mJy	VLA [e]
3.6 cm	0.23 ± 0.05 mJy	VLA [d]
6 cm	< 0.15 mJy	VLA [e]

[a]http://cobe.gsfc.nasa.gov/cio/

[b]Abbott et al. (1984)

[c]Price et al. (2001); Egan et al. (1999)

[d]This paper

[e]Drake & Linsky (1989)

2.3. *HHT Observation*

Deneb was observed using the 10-m Heinrich Hertz Telescope (e.g., Baars et al. 1999) on Mt. Graham, Arizona on 22 December 2000. We used the MPIfR 19-element bolometer array which is sensitive at 870 μm = 345 GHz. The observations were done during good weather conditions ($\tau_{225GHz} < 0.06$). We used source-sky offsets of 100$''$ compared to the telescope beam of 22.4$''$. The total on source integration time was 1600 seconds with individual integration times of 20 seconds. Mars was observed to provide calibration to physical units. While we did not detect Deneb, we were able to put a 3σ upper limit on this star of 24.0 mJy at 870 μm.

2.4. *ISO Data Reduction, DIRBE and MSX Data*

Infrared Space Observatory (ISO) observed Deneb at 60 μm with the ISOPHOT instrument (Lemke et al. 1996). This data set was downloaded from the ISO archive and reduced using the PIA package (Gabriel et al. 1997). The observations consist of three pointings bracketed by observations of the FCS1 calibration source. Each pointing was offset by almost the full array width from the last pointing and Deneb was observed in the middle pointing. Deneb was centered on the middle pixel of the array. The sky level at the position of Deneb was taken as the mean of the sky levels on the middle pixel in the two adjacent observations. The flux of Deneb was the difference between the observed flux and the sky level so computed. Including the correction for the flux falling outside the central pixel, the 60 μm flux of Deneb was 957 mJy. The uncertainty of this measurement was estimated at 30% (Schulz et al. 1999).

Infrared photometric data between 1 μm to 5 μm are from the Diffuse Infrared Background Experiment (DIRBE) aboard the Cosmic Background Explorer (COBE). These data were obtained from the Astrophysical Data Facility using the the DIRBE Point Source Photometry Research Tool. Additional infrared photometric data between 4 μm and 20 μm from the Midcourse Space Experiment (MSX) (Price et al. 2001; Egan et al. 1999) were obtained through IPAC.

2.5. *Ultraviolet Data Sources*

Spectrophotometric data of Deneb from the *Skylab* S-0109 Far-UV Objective Prism Spectrophotometer (Henize et al. 1979), the *Orbiting Astronomical Observatory-2 (OAO-2)* spectrometers (Code & Meade 1979), the S2/68 Ultraviolet Sky Survey Telescope aboard *TD1* (Jamar et al. 1976), and the *International Ultraviolet Explorer (IUE)* are all in close agreement regarding the shape and absolute flux level despite being obtained at different epochs (see Table 2). Figure 1 shows these data over their common interval from 7 μm^{-1} to 4 μm^{-1} (1400 Å to 2500 Å). The *OAO-2* data do show systematically higher fluxes relative to the other data sets between 7 μm^{-1} and 6 μm^{-1}. This *OAO-2* excess has been noted in studies on the UV spectrophotometry of B-type stars (Bohlin & Holm 1984; Aufdenberg et al. 1999) and is expected. There is good agreement between *IUE* and *OAO-2* longward of 2500 Å until the end of the LWR camera beyond 3300 Å. The only absolute spectrophotometric data shortward of 1400 Å are from *IUE*.

Only two large aperture, low dispersion spectra of Deneb were obtained with *IUE*, one each in the Short Wavelength Primary (SWP) and Long Wavelength Redundant (LWR) cameras, exposures SWP 09133 and LWR 07864, respectively. We use the *IUE* data set exclusively in our SED analysis because it has the greatest wavelength coverage, is consistent with the other UV data, has probably the best absolute (and relative) flux calibration, and both the long and short wavelength spectra were taken on the same date. For the high-dispersion analysis, we have chosen the well-exposed, large-aperture spectra SWP 10375 and LWR 07760. The *IUE* data were obtained from the ESA "IUE Newly Extracted Spectra" (INES) system (Rodríguez-Pascual et al. 1999; González-Riestra et al. 2000).

2.6. *Additional Spectroscopic and Spectrophotometric Data Sources*

TABLE 2
LOW-RESOLUTION UV SPECTROPHOTOMETRY OF DENEB

Observatory	Wavelength Range (Å)	Dates	# of Scans
OAO-2[a]	1840–3600	1969 June 19	1
OAO-2	1400–1800	1970 May 11	1
		1970 June 21	4
TD1[b]	1360–2740	1972 March 19	3
		1972 October 31	–
Skylab	1347–2290	1973 August 10	3
IUE	1150–2000	1980 May 26	1
IUE	1850–3300	1980 May 26	1

[a] *OAO-2* observation dates from Meade (2001).

[b] No observation dates available. Dates shown are those of the *TD1* mission.
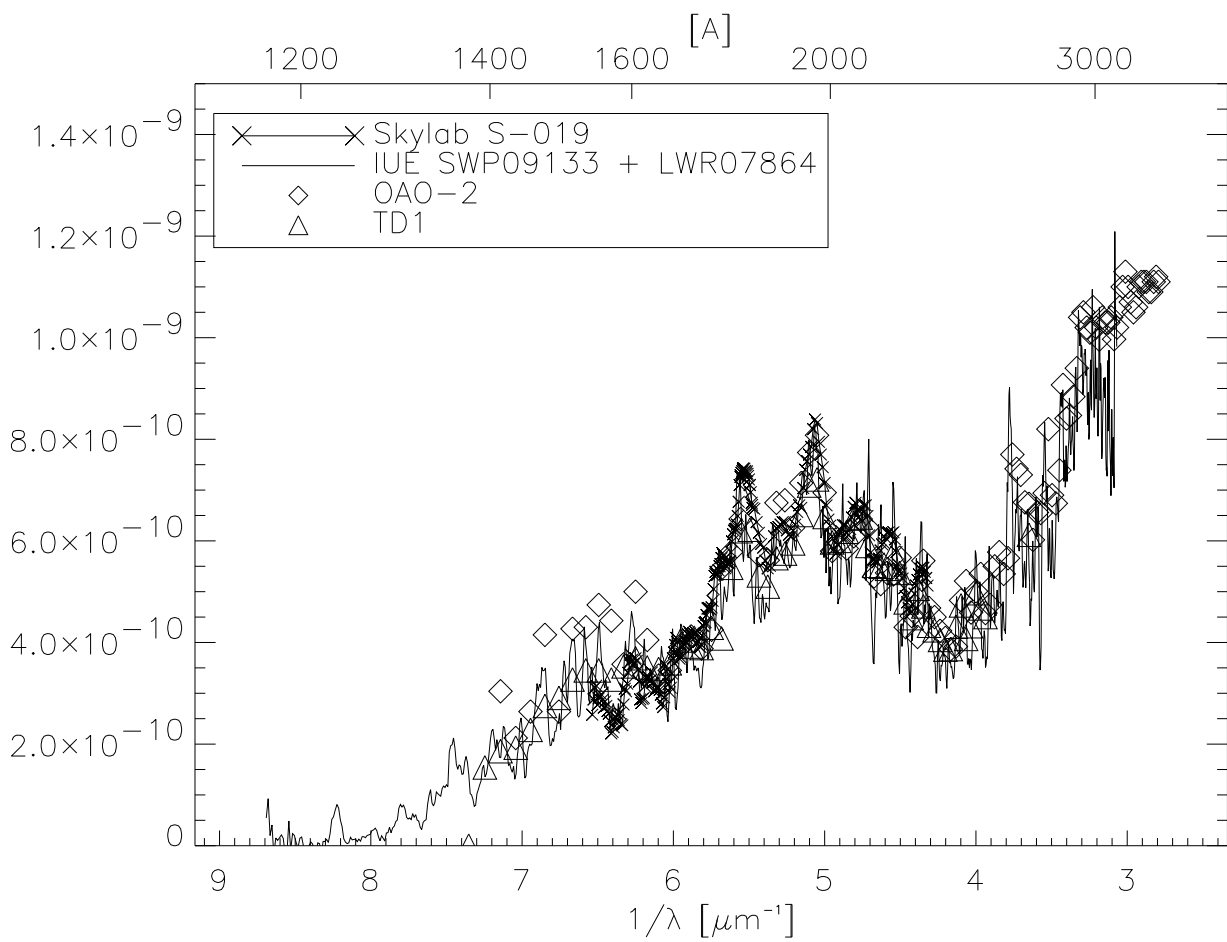
FIG. 1.— Comparison of ultraviolet absolute spectrophotometry of Deneb from *Skylab*, *IUE*, *OAO-2*, and *TD1*. See text for details.

Optical spectrophotometric data are from Glushneva et al. (1992) and are in good agreement with data from the compilation by Breger (1976) except at 3975 Å, where the datum from Glushneva et al. is $\simeq 50\%$ lower. Two high-dispersion ($R \simeq 20000$) optical spectra with wavelength coverage from 3500 Å to 5400 Å ("blue") and 5775 Å to 8630 Å ("red") were obtained on 1 August 1995 with the Heidelberg echelle spectrograph HEROS (Kaufer 1999). Fourier Transform Spectroscopy ($R \simeq 3000$) in the K-band is from Wallace & Hinkle (1997).

2.7. *NPOI Observations*

Each interferometric observation consists of a scan made over ten spectral channels spread in increments of equal wavenumber from 850 nm to 650 nm with a mean wavelength of 740 nm. Here we consider only the visibility data from the 38-meter East-West baseline, considered the most robust (Nordgren et al. 1999). Deneb was observed 74 times over 5 nights in 1997 December. Unfortunately, 62 of these observations have no suitable calibration data. Of the remaining data, 5 scans from 1997 December 5, 7 scans from 1997 December 6, and 1 scan from 1997 December 16 have suitable calibration data taken within one hour of each science scan. These data are listed in Table 3 and plotted in Figure 2. The calibration star for each night and its estimated angular size (Nordgren et al. 1999) are noted in Table 3. For a detailed description of the calibration process used for these data see Nordgren et al. (1999).

TABLE 3
NPOI Deneb Observations

Observation Time (UT)	Cal. Time[a] (hours)	Wavelength (nm)	V^2		Spatial Frequency (cycles/arcsecond)
			1997 December 5[b]		
01:40:05	0.305	849.4	0.5778 ±	0.0075	195.5441
01:40:05	0.305	820.9	0.5572	0.0074	202.3308
01:40:05	0.305	793.9	0.5155	0.0073	209.2131
01:40:05	0.305	768.3	0.5089	0.0080	216.1828
01:40:05	0.305	744.2	0.4803	0.0072	223.1807
01:40:05	0.305	722.9	0.4605	0.0073	229.7603
01:40:05	0.305	701.5	0.4388	0.0064	236.7691
01:40:05	0.305	683.1	0.4165	0.0068	243.1457
01:40:05	0.305	664.6	0.3947	0.0063	249.9149
01:40:05	0.305	648.9	0.3704	0.0066	255.9606
01:52:05	0.505	849.4	0.5914	0.0078	192.7878
01:52:05	0.505	820.9	0.5689	0.0079	199.4806
01:52:05	0.505	793.9	0.5279	0.0074	206.2675
01:52:05	0.505	768.3	0.5210	0.0083	213.1379
01:52:05	0.505	744.2	0.4962	0.0075	220.0392
01:52:05	0.505	722.9	0.4759	0.0074	226.5235
01:52:05	0.505	701.5	0.4544	0.0068	233.4355
01:52:05	0.505	683.1	0.4302	0.0076	239.7208
01:52:05	0.505	664.6	0.4045	0.0065	246.3961
01:52:05	0.505	648.9	0.3910	0.0068	252.3545
01:59:49	0.634	849.4	0.5929	0.0079	190.9612
01:59:49	0.634	820.9	0.5655	0.0081	197.5905
01:59:49	0.634	793.9	0.5261	0.0076	204.3120
01:59:49	0.634	768.3	0.5197	0.0084	211.1178
01:59:49	0.634	744.2	0.4928	0.0078	217.9575
01:59:49	0.634	722.9	0.4733	0.0078	224.3784
01:59:49	0.634	701.5	0.4519	0.0071	231.2249
01:59:49	0.634	683.1	0.4297	0.0078	237.4519
01:59:49	0.634	664.6	0.4079	0.0068	244.0599
01:59:49	0.634	648.9	0.3907	0.0074	249.9678
02:12:32	0.846	849.4	0.5999	0.0086	187.9221
02:12:32	0.846	820.9	0.5776	0.0082	194.4449
02:12:32	0.846	793.9	0.5388	0.0080	201.0607
02:12:32	0.846	768.3	0.5376	0.0089	207.7591
02:12:32	0.846	744.2	0.5136	0.0084	214.4886
02:12:32	0.846	722.9	0.4924	0.0080	220.8083
02:12:32	0.846	701.5	0.4722	0.0074	227.5415
02:12:32	0.846	683.1	0.4481	0.0085	233.6719
02:12:32	0.846	664.6	0.4306	0.0071	240.1741
02:12:32	0.846	648.9	0.4116	0.0076	245.9880
			1997 December 6[c]		
01:16:52	0.087	849.4	0.4991 ±	0.0100	199.7180
01:16:52	0.087	820.9	0.4534	0.0088	206.6525
01:16:52	0.087	793.9	0.4377	0.0090	213.6804
01:16:52	0.087	768.3	0.4091	0.0107	220.8014
01:16:52	0.087	744.2	0.3942	0.0095	227.9508
01:16:52	0.087	722.9	0.3724	0.0091	234.6640
01:16:52	0.087	701.5	0.3710	0.0088	241.8242
01:16:52	0.087	683.1	0.3338	0.0095	248.3401
01:16:52	0.087	664.6	0.3138	0.0088	255.2507
01:16:52	0.087	648.9	0.2957	0.0084	261.4261
01:44:35	0.074	849.4	0.6075	0.0103	193.6147
01:44:35	0.074	820.9	0.5023	0.0075	200.3382
01:44:35	0.074	793.9	0.4984	0.0077	207.1531
01:44:35	0.074	768.3	0.4752	0.0085	214.0514
01:44:35	0.074	744.2	0.4401	0.0081	220.9846
01:44:35	0.074	722.9	0.4189	0.0078	227.4956
01:44:35	0.074	701.5	0.4107	0.0077	234.4356
01:44:35	0.074	683.1	0.3948	0.0074	240.7516
01:44:35	0.074	664.6	0.3711	0.0076	247.4509
01:44:35	0.074	648.9	0.3683	0.0081	253.4416
02:14:50	0.048	849.4	0.5821	0.0094	187.9029
02:14:50	0.048	820.9	0.5490	0.0084	194.4257
02:14:50	0.048	793.9	0.5181	0.0086	201.0415
02:14:50	0.048	768.3	0.5153	0.0093	207.7393
02:14:50	0.048	744.2	0.4667	0.0085	214.4687
02:14:50	0.048	722.9	0.4568	0.0085	220.7885
02:14:50	0.048	701.5	0.4567	0.0092	227.5210
02:14:50	0.048	683.1	0.4371	0.0083	233.6514
02:14:50	0.048	664.6	0.4057	0.0083	240.1537
02:14:50	0.048	648.9	0.4228	0.0095	245.9638
02:27:25	0.054	849.4	0.6579	0.0140	183.3663
02:27:25	0.054	820.9	0.6186	0.0130	189.7327
02:27:25	0.054	793.9	0.5967	0.0127	196.1848
02:27:25	0.054	768.3	0.6022	0.0138	202.7225

A uniform-disk (UD) angular diameter θ_{UD} was derived for each calibrated scan by fitting an Airy pattern

$$V^2(kw) = \left[\frac{J_1(2kw\alpha_{\mathrm{UD}})}{kw\alpha_{\mathrm{UD}}} \right]^2 \tag{1}$$

to the visibility data, where kw is the spatial frequency, $k = 2\pi/\lambda$ is the wavenumber and w is the projected baseline, $\alpha_{\mathrm{UD}} = \theta_{\mathrm{UD}}/2$ is the angular radius, and J_1 is the Bessel function of first order. Table 4 lists the least squares best fit value of θ_{UD} for each scan and the mean value of θ_{UD} for each night. The model visibility curves corresponding to the mean and $\pm 1\sigma$ values of θ_{UD} for each night are shown in Figure 2.

The scans of December 5th are very consistent with each other and with the single scan from December 16th which, while noisier, yields a consistent angular diameter. The scans from December 6th, however, show considerable scatter and each scan is considerably noiser than the December 5th data, yielding higher χ^2 values for each of the fits. A histogram of all the derived θ_{UD} values is shown in Figure 3. Experience has shown that with well-observed stars the distribution of angular diameters follows a Gaussian distribution in the limit of many ($\sim$100) scans. The weighted mean angular diameter for the 12 scans is

$$\overline{\theta_{\mathrm{UD}}} = 2.40 \pm 0.06 \text{ mas}, \tag{2}$$

where the uncertainty represents our estimate for the error in the mean. This value is consistent with the published measurements by the CERGA group: $\theta_{\mathrm{UD}} = 2.04 \pm 0.45$ mas (in the spectral band 600 ± 25 nm) (Koechlin & Rabbia

TABLE 3—*Continued*

Observation Time (UT)	Cal. Time[a] (hours)	Wavelength (nm)	V^2		Spatial Frequency (cycles/arcsecond)
02:27:25	0.054	744.2	0.5811	0.0133	209.2878
02:27:25	0.054	722.9	0.5517	0.0132	215.4553
02:27:25	0.054	701.5	0.5787	0.0142	222.0274
02:27:25	0.054	683.1	0.5387	0.0135	228.0098
02:27:25	0.054	664.6	0.5204	0.0142	234.3555
02:27:25	0.054	648.9	0.5041	0.0135	240.0260
02:51:50	0.060	849.4	0.6771	0.0187	177.5475
02:51:50	0.060	820.9	0.6405	0.0166	183.7125
02:51:50	0.060	793.9	0.6047	0.0155	189.9600
02:51:50	0.060	768.3	0.6327	0.0190	196.2900
02:51:50	0.060	744.2	0.5964	0.0165	202.6481
02:51:50	0.060	722.9	0.5696	0.0163	208.6200
02:51:50	0.060	701.5	0.6360	0.0245	214.9848
02:51:50	0.060	683.1	0.5725	0.0190	220.7742
02:51:50	0.060	664.6	0.5513	0.0199	226.9180
02:51:50	0.060	648.9	0.5760	0.0217	232.4076
03:18:22	0.065	849.4	0.5428	0.0099	171.7017
03:18:22	0.065	820.9	0.5794	0.0111	177.6646
03:18:22	0.065	793.9	0.5567	0.0108	183.7040
03:18:22	0.065	768.3	0.5434	0.0119	189.8256
03:18:22	0.065	744.2	0.5123	0.0103	195.9740
03:18:22	0.065	722.9	0.5012	0.0110	201.7472
03:18:22	0.065	701.5	0.5088	0.0111	207.9038
03:18:22	0.065	683.1	0.4848	0.0119	213.5034
03:18:22	0.065	664.6	0.4523	0.0111	219.4446
03:18:22	0.065	648.9	0.4825	0.0128	224.7564
03:44:02	0.095	849.4	0.6227	0.0121	166.8693
03:44:02	0.095	820.9	0.5874	0.0107	172.6637
03:44:02	0.095	793.9	0.5863	0.0124	178.5318
03:44:02	0.095	768.3	0.5590	0.0121	184.4802
03:44:02	0.095	744.2	0.5377	0.0115	190.4547
03:44:02	0.095	722.9	0.5383	0.0123	196.0689
03:44:02	0.095	701.5	0.5341	0.0125	202.0478
03:44:02	0.095	683.1	0.5186	0.0111	207.4907
03:44:02	0.095	664.6	0.4895	0.0127	213.2697
03:44:02	0.095	648.9	0.4918	0.0150	218.4261
		1997 December 16[d]			
01:03:29	0.214	849.4	0.5761 $\pm$	0.0216	194.0322
01:03:29	0.214	820.9	0.5435	0.0134	200.7689
01:03:29	0.214	793.9	0.5133	0.0142	207.5969
01:03:29	0.214	768.3	0.5163	0.0155	214.5110
01:03:29	0.214	744.2	0.4526	0.0129	221.4574
01:03:29	0.214	722.9	0.4671	0.0129	227.9843
01:03:29	0.214	701.5	0.5164	0.0184	234.9374
01:03:29	0.214	683.1	0.4550	0.0148	241.2693
01:03:29	0.214	664.6	0.4434	0.0153	247.9844
01:03:29	0.214	648.9	0.4804	0.0193	253.9841

[a] Time between the science source scan and the calibration scan used to calibrate it.

[b] Calibration: γ Peg, $\theta_{\mathrm{UD}} = 0.421$ mas

[c] Calibration: α Lac, $\theta_{\mathrm{UD}} = 0.502$ mas

[d] Calibration: ζ Cas, $\theta_{\mathrm{UD}} = 0.264$ mas
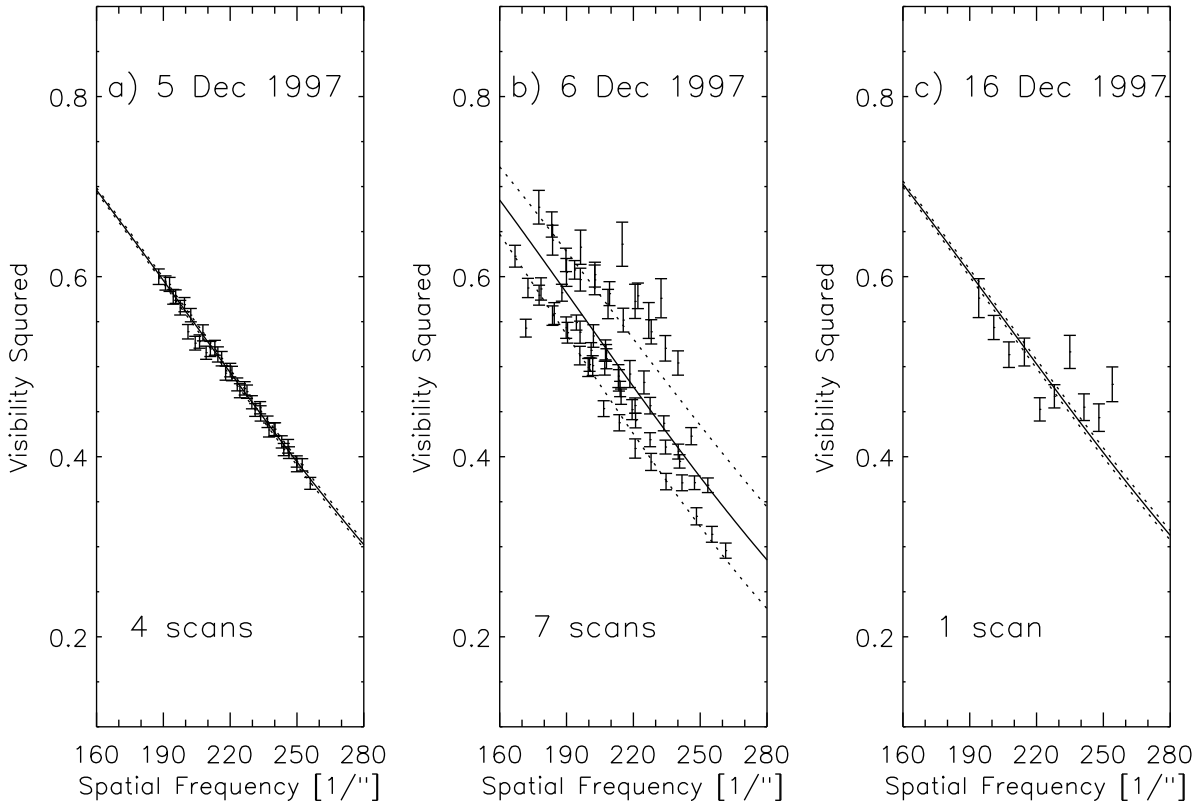
FIG. 2.— NPOI visibility data of Deneb with uniform-disk (UD) fits. For each date, a model visibility curve (solid line) for the mean UD diameter, $\overline{\theta_{UD}}$ (see Table 4), is plotted along with the corresponding visibility curves for the $\pm 1\sigma$ error in the mean UD diameter (dotted lines). (a) 5 December 1997: $\overline{\theta_{UD}} = 2.36 \pm 0.01$ mas (4 scans); (b) 6 December 1997: $\overline{\theta_{UD}} = 2.41 \pm 0.17$ mas (7 scans); (c) 16 December 1997: $\theta_{UD} = 2.33 \pm 0.02$ mas (1 scan).

TABLE 4
UNIFORM-DISK ANGULAR DIAMETERS

Observation Time (UT)	θ_{UD} (mas)	χ^2
1997 December 5: $\overline{\theta_{UD}} = 2.364 \pm 0.011$		
01:40:05	2.364 ± 0.007	4.7
01:52:05	2.353 ± 0.007	5.0
01:59:49	2.379 ± 0.007	4.9
02:12:32	2.360 ± 0.008	7.1
1997 December 6: $\overline{\theta_{UD}} = 2.410 \pm 0.168$		
01:16:52	2.578 ± 0.009	17
01:44:35	2.470 ± 0.008	57
02:14:50	2.432 ± 0.009	38
02:27:25	2.180 ± 0.014	20
02:51:50	2.169 ± 0.020	30
03:18:22	2.541 ± 0.012	90
03:44:02	2.501 ± 0.014	32
1997 December 16: $\theta_{UD} = 2.325 \pm 0.015$		
01:03:29	2.325 ± 0.015	61

1985) and $\theta_{\rm UD} = 2.6 \pm 0.3$ mas (in the spectral range 500-650 nm) (Bonneau et al. 1981). Hanbury Brown's interferometer at Narrabri could not observe Deneb due to its high declination.

3. ANGULAR DIAMETER

Our model atmospheres (described in detail in Appendix A) predict substantial limb darkening for the Deneb parameters determined in the remainder of this paper. This motivates further analysis of the NPOI observations in order to obtain a more physically based estimate of the angular diameter. A limb-darkened angular diameter, $\theta_{\rm LD}$, is normally employed in the calculation of the fundamental effective temperature

$$T_{\rm eff} = \left[\frac{4\mathcal{F}_0}{\sigma \theta_{\rm LD}^2} \right]^{1/4}. \tag{3}$$

where $\mathcal{F}_0$ is the bolometric flux (corrected for interstellar extinction) and σ is the Stefan-Boltzmann constant. Unfortunately, in extended atmospheres the effective temperature is not well defined or is ambiguous because the atmosphere is not sufficiently compact to have a unique radius (Baschek et al. 1991). Hence, a value for $T_{\rm eff}$ cannot be separated from an adopted value for the radius and the corresponding angular size.

For well resolved sources (e.g., Betelgeuse, Arcturus), observations can directly yield limb-darkening information from the shape of the visibility curve at spatial frequencies beyond the first null. Deneb, however, has yet to be observed at sufficiently long baselines (> 100 m) for limb-darkening information to be obtained in this way. Therefore, the details of Deneb's center-to-limb variation (CLV) must for now be supplied by theory.

Limb-darkening coefficients provided in the literature (e.g., Claret (2000)) are derived from plane-parallel models and are not appropriate for Deneb. For example, Figure 4a shows that the model CLV from an expanding atmosphere or "wind" model differ significantly from that of a hydrostatic model. Unlike the wind model CLV which falls very gradually from 40% of the central disk intensity to zero, the hydrostatic model CLV shows a fairly well defined edge. The unambiguous signature of the predicted wind model CLV lies in the height of the visibility function beyond the first null (see Figure 4b). Future measurements should be able to test this prediction.
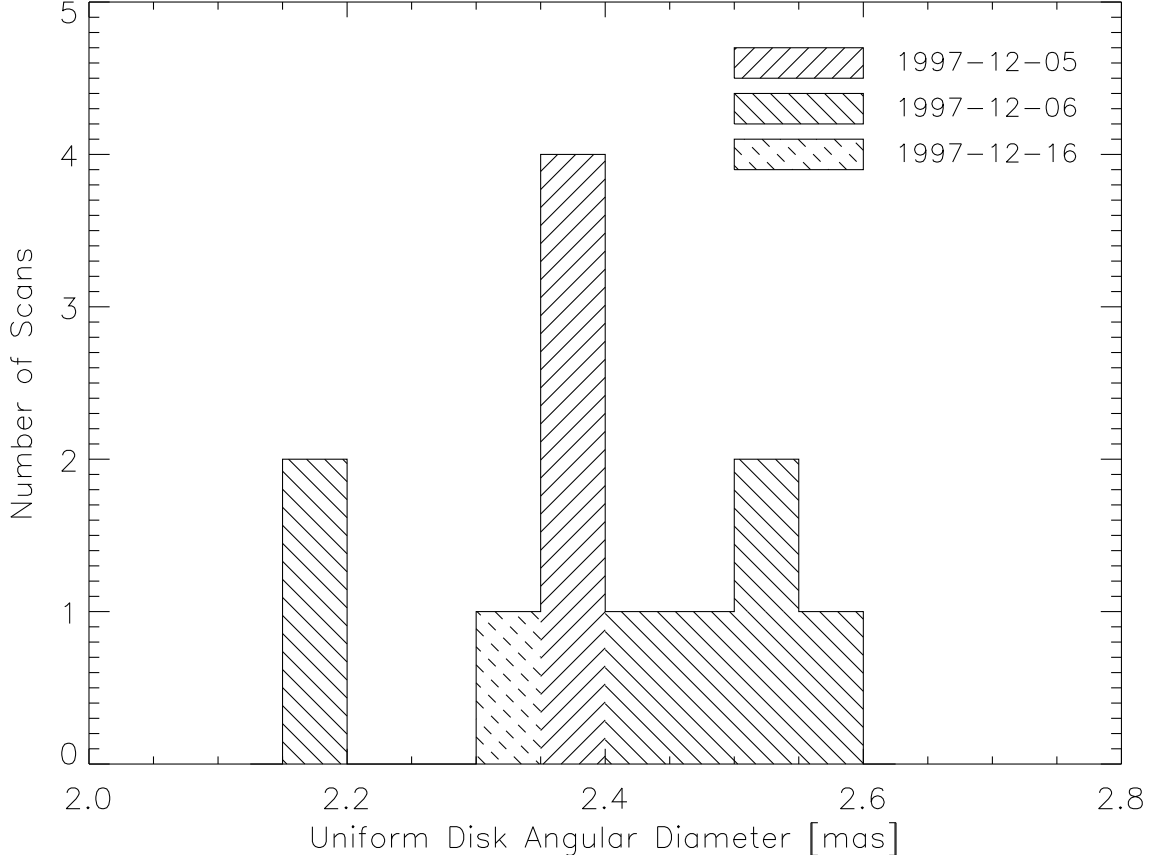
Fig. 3.— Histogram of the uniform-disk angular diameter values derived from each of the 12 scans of Deneb by the NPOI (see Table 4). The data are binned to 0.05 mas. The different cross-hatched regions specify the date of each scan.

The gradual decline of the wind model CLV presents a problem for deriving $\theta_{\rm LD}$. As noted by Baschek et al. (1991), a flat intensity decrease toward the outer disk leaves an "intensity radius", defined by an arbitrary cutoff of the CLV, e.g. at 1%, poorly defined. Such a profile prohibits a simple relation between an "optical depth radius", which corresponds to reference optical depth along a ray normal to the atmosphere, and an "intensity radius", which corresponds to the impact parameter of a ray at the angle of the intensity cutoff. We choose to define the limb-darkened edge to be the angle beyond which the model intensity profile would have an immeasurable effect on the observed visibilities. This is defined quantitatively by the following procedure.

The intensity of the stellar disk as a function of the angular radius, $I(\alpha)$, is extracted from the model atmosphere. The coordinate system for the solution of the spherical model atmosphere problem is specified by a set of parallel rays tangent to nested spherical shells (e.g., see Figure 1 in Hummer & Rybicki 1971; Mihalas et al. 1975). The rays are parameterized by the perpendicular distance p from the line of symmetry though the center of the star. A solution to the model atmosphere problem provides the specific intensity I_λ at wavelength λ at depths z along each ray. The observed intensity for a given ray is taken to be the intensity at the intersection of that ray with the outermost shell. The relation between the directional cosine of the emergent radiation, $\mu = \cos\theta$, and the angular displacement on the sky, α, is

$$\alpha = (1 - \mu^2)^{1/2}. \tag{4}$$

The spectral response of the NPOI is approximated by the mean the R- and I-bands (Nordgren et al. 1999). Hence, after calculating $I_\lambda(\alpha)$ on a fine wavelength grid, a passband-weighted CLV for each filter,

$$\bar{I}_i(\alpha) = \frac{\int_{a_i}^{b_i} I_\lambda(\alpha)S_i(\lambda)\,d\lambda}{\int_{a_i}^{b_i} S_i(\lambda)\,d\lambda} \tag{5}$$

is computed, where $S_i(\lambda)$ is the response function of the photometric system for the filter i with wavelength limits a_i and b_i. Response functions for the V-, R- and I-bands are taken from Bessell (1990).

Following Quirrenbach et al. (1996), the model visibilities, $V_i(kw)$, for each passband are computed by numerically integrating

$$V_i^2(kw) = \left[2\pi \int_0^{\alpha_{\rm limb}} J_0(kw\alpha)\bar{I}_i(\alpha)\alpha\,d\alpha\right]^2 \tag{6}$$

where $\alpha_{\rm limb} = \alpha_{\rm LD} = \theta_{\rm LD}/2$ is the limb-darkened angular radius and J_0 is the Bessel function of zeroth order. The squared visibility will be insensitive to the low-intensity tail of the CLV beyond some angle. Therefore, we define $\alpha_{\rm limb}$ to be the angle beyond which the CLV affects the visibility at 220 arcsec^{-1} by less than 1%, approximately the precision of the NPOI observations. This corresponds to an intensity cutoff at $\sim$5% of the central disk intensity (see Figure 5a).

Figure 5b shows that well inside the first null, the shapes of UD and LD visibility curves are essentially identical and both fit the NPOI data, but correspond to quantitatively different diameters, $\theta_{\rm UD}$ and $\theta_{\rm LD}$, respectively. The ratio $\theta_{\rm LD}/\theta_{\rm UD} = \alpha_{\rm LD}/\alpha_{\rm UD}$ is the limb-darkening correction. The value of $\alpha_{\rm UD}$ parameterizes the UD visibility curve, equation (1). The average limb-darkening correction from the R- & I-bands is 15.0%. Therefore, we adopt

$$\theta_{\rm LD} = 1.15 \cdot \theta_{\rm UD} = 2.76 \pm 0.06 \text{ mas} \tag{7}$$

as the limb-darkened angular diameter of Deneb.

An accurate and precise limb-darkened angular diameter measurement may yield an effective temperature, via equation (3), which is not consistent with the visual color temperature or previously determined values for $T_{\rm eff}$ from model atmosphere fitting. A proper interpretation of this $T_{\rm eff}$ can be made only after an appropriate CLV has been modeled (or measured) and the relationships between the intensity and optical depth radii have been established. Three different radii, and their corresponding angular diameters, are useful for the comparison of our model atmospheres with the observational data: (1) $R_\star$, the input radius to the model atmosphere, $L = 4\pi R_\star^2 \sigma T_\star^4$, which also corresponds to the radius at the base of the wind (see §A.2.2); (2) $R(\tau_{\rm Ross} = 2/3)$, the optical depth radius corresponding a Rosseland optical depth of 2/3; (3) $R_{\rm limb}$, the wavelength-dependent radius corresponding to the limb-darkened edge of the atmosphere, the impact parameter at the angle $\alpha_{\rm limb}$.

An example of the relationship between these radii is provided by one of the best fitting models to Deneb's spectral energy distribution (see Table 6, §5.2). For this model the ratio $R_{\rm limb}/R(\tau_{\rm Ross} = 2/3) = 1.19$. This says that the intensity radius derived from the CLV is 19% larger than the optical depth radius in the V-band. Furthermore, this model is parameterized with $R_\star$, where $R_\star/R(\tau_{\rm Ross} = 2/3) = 0.89$, and $T_\star = 9000$ K. Therefore, the effective temperature corresponding to $R_{\rm limb}$ and the same luminosity is

$$T_{\rm eff}^{\rm limb} = T_\star \sqrt{R_\star/R_{\rm limb}} = 7780 \text{ K}. \tag{8}$$

This model effective temperature can be directly compared to $T_{\rm eff}$ from equation 3. However, $T_{\rm eff}^{\rm limb}$ is not the most physically relevant temperature and it can be easily shown that a plane-parallel, hydrostatic model with this effective temperature is a very poor match to the spectral energy distribution.

The most useful effective temperature is one which corresponds to the radius at a Rosseland optical depth of $\tau_{\rm Ross} = 2/3$. In this model, the V-, R- and I-band optical depth radii all differ by less than 1% from the Rosseland depth. The corresponding effective temperature is

$$T_{\rm eff}^{\rm Ross} = T_\star \sqrt{R_\star/R(\tau_{\rm Ross} = 2/3)} \simeq 8490 \text{ K}. \tag{9}$$
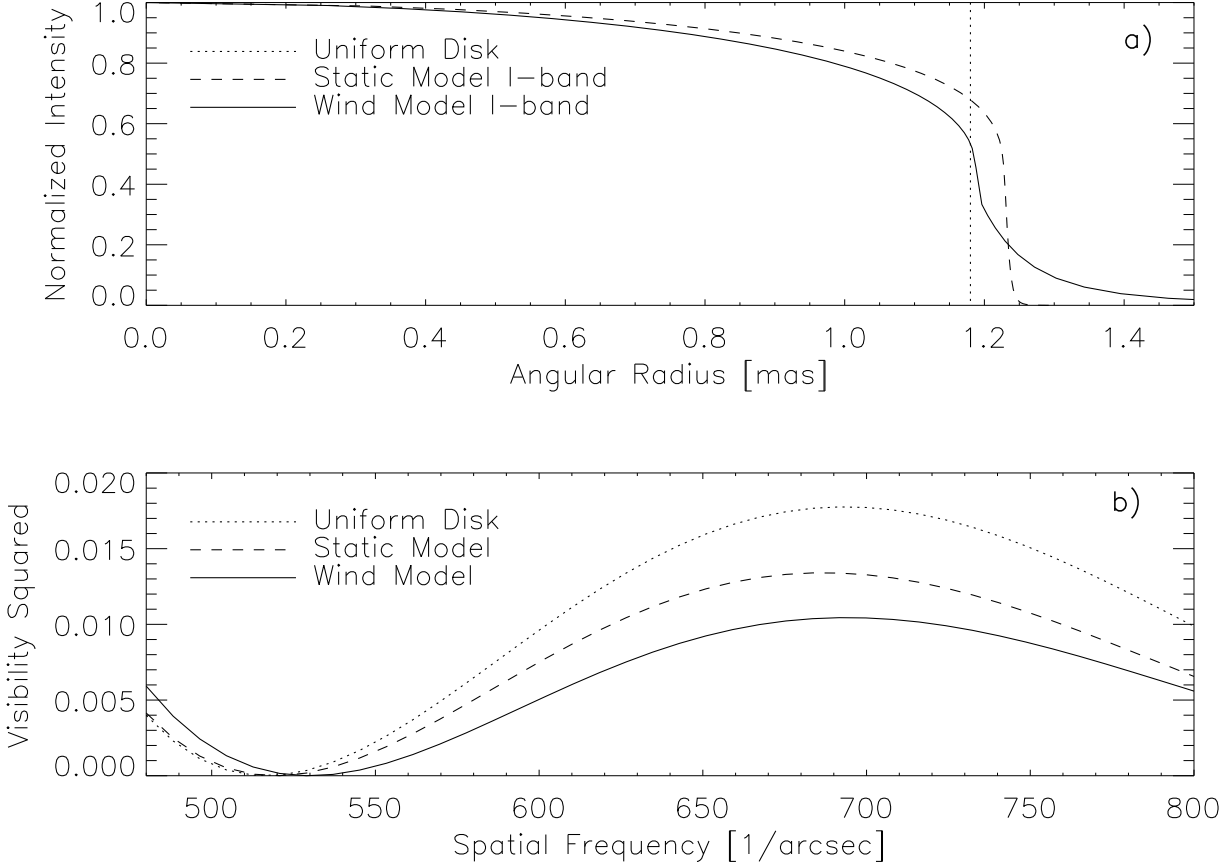
Fig. 4.— (a) Comparison of the I-band center-to-limb variations (CLVs) from two model atmospheres and a uniform-disk: uniform-disk (dotted line), spherical, hydrostatic model (dashed line), and spherical hydrostatic plus expanding wind model (solid line). The three CLVs have been scaled so that their visibility curves match the NPOI data from 5 December 1997 at 220 arcsec^{-1}. (b) Different CLVs can be most easily discriminated beyond the first null; the uniform-disk squared visibilities are predicted to be 60% larger than the wind model squared visibilities at a spatial frequency of 700 arcsec^{-1} in the I-band. The spherical, expanding atmosphere model is parameterized by: $T_\star = 9000$ K at $R_\star = 1.2 \times 10^{13}$ cm and a surface gravity, $\log g(R_\star) = 1.3$, equivalent to $T_{\rm eff} = 8543$ K at $R(\tau_{\rm Ross} = 2/3)$ and $\log g(R) = 1.21$, see equation 9; a mass-loss rate, $\dot{M} = 5.0 \times 10^{-7}$ M$_\odot$ yr^{-1}; a terminal wind velocity, $v_\infty = 225$ km s^{-1}; and a velocity law exponent, $\beta = 3.0$ (see §A.2). The spherical, hydrostatic model is parameterized by: $T_\star = 8500$ K at $R_\star = 1.2 \times 10^{13}$ cm and $\log g(R_\star) = 1.3$, equivalent to $T_{\rm eff} = 8746$ K at $R(\tau_{\rm Ross} = 2/3)$ and $\log g(R) = 1.35$.
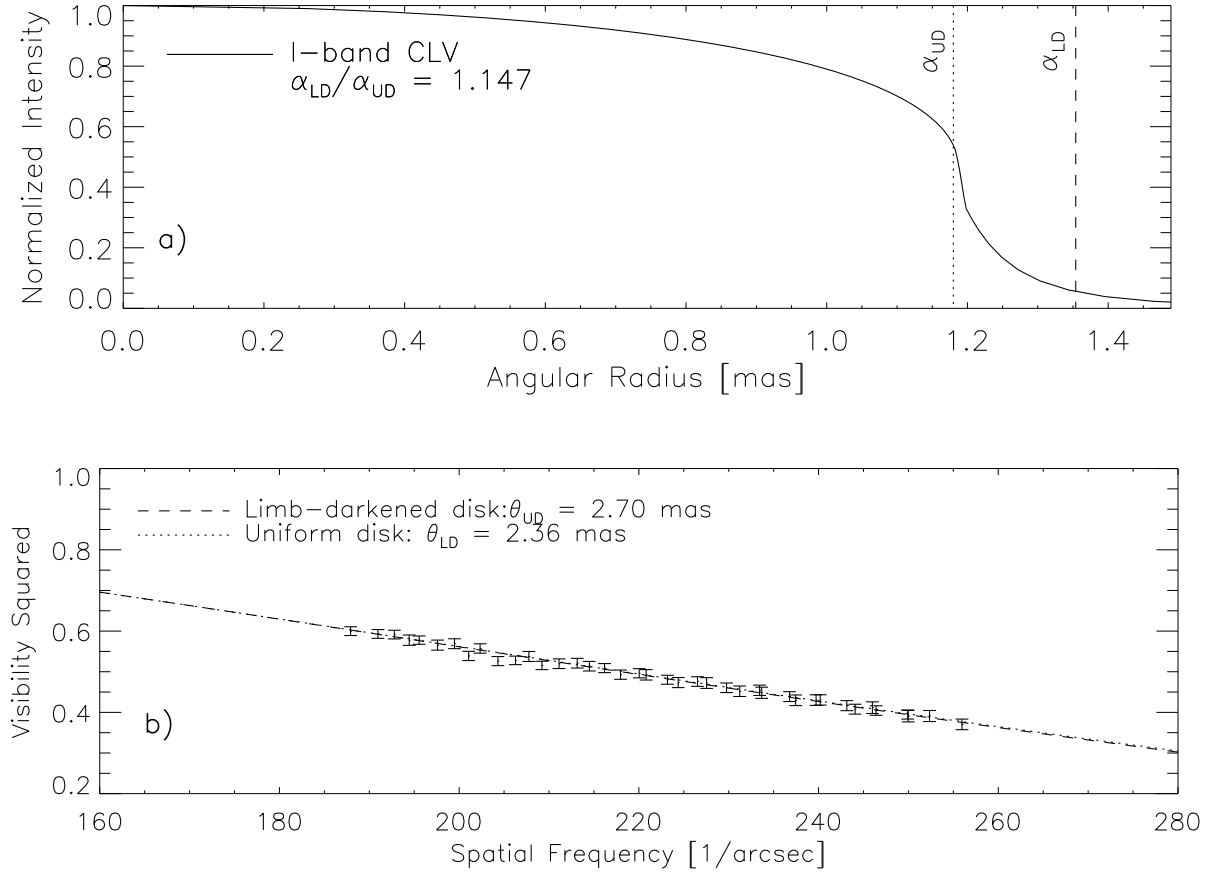
FIG. 5.— (a) Model center-to-limb variation in the I-band for an spherical, expanding atmosphere model with parameters: $T_\star = 9000$ K at $R_\star = 1.2 \times 10^{13}$ cm and $\log g(R_\star) = 1.3$, equivalent to $T_{\rm eff} = 8490$ K at $R(\tau_{\rm Ross} = 2/3)$ and $\log g(R) = 1.19$, see equation 9; $\dot{M}$ = 1.0×10^{-6} M$_\odot$ yr^{-1}; $v_\infty = 225$ km s^{-1}; and $\beta = 3.0$. The vertical dashed line, labeled $\alpha_{\rm LD}$, marks the angular radius beyond which $\Delta V^2(220 \text{ arcsec}^{-1}) < 1\%$ (see text) . The dotted line, labeled $\alpha_{\rm UD}$, marks the angular radius of a uniform-disk with a visibility curve that matches the limb-darkened visibility curve at $V^2 = 0.5$. For this model the limb-darkened radius is 15% larger than the uniform-disk radius. (b) Corresponding visibility curves for the model I-band CLVs (dashed, limb-darkened disk; dotted, uniform-disk) over plotted on the visibilities measured by NPOI on 1997 December 5.

Interestingly, the ratio $R_{\rm limb}/R(\tau_{\rm Ross} = 2/3)$ is larger than the limb-darkening correction, $\alpha_{\rm LD}/\alpha_{\rm UD}$. This means that the angular diameter corresponding to $T_{\rm eff}^{\rm Ross}$ is *smaller* than the uniform-disk diameter.

$$\theta_{\rm Ross} = \theta_{\rm LD} \frac{R(\tau_{\rm Ross} = 2/3)}{R_{\rm limb}} = 2.32 \pm 0.06 \text{ mas} \tag{10}$$

With more compact stars, the limb-darkening correction is used to scale up the angular diameter from the uniform-disk measurement ($\theta_{\rm Ross} > \theta_{\rm UD}$) in order to bring the fundamental effective temperature in line with the color temperature. However, in the case of Deneb (and likely for other BA-supergiants) the angular diameter must be scaled down from uniform-disk measurement ($\theta_{\rm Ross} < \theta_{\rm UD}$) for this purpose. In effect, the observed uniform-disk diameter is biased toward a larger diameters than it otherwise would be in the absence of the gradual drop-off in the center-to-limb profile predicted by our wind models. Longer baseline interferometry of Deneb is needed to test this prediction.

4. OBSERVATIONAL CONSTRAINTS

4.1. *Effective Temperature and Reddening*

The most fundamental atmospheric parameter of a stellar atmosphere is its effective temperature. As shown above, $T_{\rm eff}$ must be carefully defined in the case of an extended atmosphere. Published values for Deneb's $T_{\rm eff}$ range from 7635 K to 10080 K (Verdugo et al. 1999). Efforts to establish an accurate and precise value of $T_{\rm eff}$ have been ongoing for the last thirty years. Constraints on Deneb's fundamental effective temperature have been limited by the large uncertainties in its angular diameter and in the foreground extinction which enters into the calculation through the bolometric flux. As a result, the value of $T_{\rm eff}$ determined from the bolometric flux and the angular diameter, has been uncertain at a level of $\sim 30\%$. We can now use the more precise ($\sim 3\%$) angular diameter obtained by NPOI to better constrain both $T_{\rm eff}$ and the foreground extinction.

The extinction curve toward Deneb is not well established due to the lack of nearly unreddened A-type supergiants with which to perform a pair method extinction curve analysis. As a best guess, we have used an extinction curve derived for the well-studied line-of-sight toward the O9 V((f)) star HD 199579 (Fitzpatrick & Massa 1990). Deneb and HD 199579 lie in the same extinction field, demarcated (84/0.0) by Neckel et al. (1980). The correlation (Jenniskens & Greenberg 1993) between the linear slope component ($c_2 = 0.898$ for HD 199579, Fitzpatrick & Massa 1990) of the UV extinction curve and R_V, the ratio of total to selective extinction, is

$$R_V = (4.61 \pm 0.22) - (1.89 \pm 0.34)c_2 \tag{11}$$

which yields,

$$R_V = 2.9 \pm 0.5. \tag{12}$$

The color excess, $E(B-V)$, toward Deneb is not well constrained in the literature. Published values range from 0.04 (Weaver & Torres-Dodgen 1995) to 0.10 (Takeda 1994) to 0.15 (Welty et al. 1994; Abbott et al. 1984). The NPOI angular diameter, corrected to the V-band (equation 10), allows us to estimate $E(B-V)$ through the empirical surface brightness to intrinsic $(V-R)$ color relation of Barnes et al. (1976). This is done by finding a simultaneous solution to the V-band surface brightness

$$F_V = 4.2207 - 0.1V_0 - 0.5\log\theta_{\rm Ross} \tag{13}$$

and the Barnes-Evans relation in the color range appropriate for Deneb:

$$F_V = 3.977 - 1.390(V-R)_0, \qquad -0.17 \leq (V-R)_0 \leq 0.00 \tag{14}$$

These two equations can be expressed in terms of the observed V magnitude, the observed $(V-R)$ color, and $E(B-V)$:

$$F_V = 4.2207 - 0.1\Big[V - R_V \cdot E(B-V)\Big] - 0.5\log\theta_{\rm Ross} \tag{15}$$

$$F_V = 3.977 - 1.390\Big[(V-R) - 0.82E(B-V)\Big] \tag{16}$$

using the relationship $E(V-R) = 0.82E(B-V)$ from Barnes et al. (1978). With the observed V and R magnitudes (Johnson et al. 1966) and R_V (equation 12) the solution equations (15) and (16) yields

$$E(B-V) = 0.09^{+0.04}_{-0.03} \tag{17}$$

The uncertainty in $E(B-V)$ is primarily due to the scatter (0.025 mag) in the Barnes-Evans relation, but also to the uncertainties in $\theta_{\rm Ross}$ and R_V. This method of estimating the reddening yields a best estimate for $E(B-V)$; however the range of uncertainty still corresponds to the range of values in the literature.

With best estimates for the angular diameter and reddening we proceed calculate Deneb's effective temperature. The UV extinction curve of HD 199579 is used to deredden Deneb's UV spectrum, while the optical data are dereddened using the extinction relations from Cardelli et al. (1989). The bolometric flux is calculated by integrating the dereddened UV and optical spectrophotometric data from 1150 Å to 10725 Å. Fluxes at longer and shorter wavelengths provide a negligible contribution to the bolometric flux. Spectra SWP08133 and LWP07864 were used for the range 1150 Å $\leq \lambda <$ 3260 Å, and the optical and near-infrared data from Glushneva et al. (1992) were used for the range 3260 Å $\leq \lambda \leq$ 10750 Å. The uncertainty in the bolometric flux is primarily a combination of uncertainties in the extinction, the monochromatic flux measurements, and the absolute flux calibrations. Absolute calibration uncertainties are taken to be 10% in the UV and 5% in the optical, while uncertainties in the angular diameter and extinction are taken from equations (10), (12), and (17) respectively. This yields a fundamental effective temperature for Deneb of

$$T_{\rm eff}^{\rm Ross} = 8600 \pm 500 \text{ K.} \tag{18}$$

4.2. *Photospheric Radius and Gravity*

Taking the Rosseland mean angular diameter of Deneb from equation (10) and the mean *Hipparcos* parallax, $\pi = 1.01 \pm 0.57$ mas (Perryman et al. 1997), yields a radius of $R(\tau_{\mathrm{Ross}} = 2/3) \simeq 1.7 \times 10^{13}$ cm $= 240\ R_{\odot}$. The large uncertainty in the parallax causes the distance probability distribution function to have a long tail extending to large distances. If the most probable value from the distance probability distribution function is adopted (685 pc, as opposed to the mean, 990 pc), the radius is $R(\tau_{\mathrm{Ross}} = 2/3) \simeq 1.2 \times 10^{13}$ cm $= 172\ R_{\odot}$.

Humphreys (1978) assigns Deneb to the Cyg OB7 association, with an adopted true distance modulus of 9.5 (794 pc), which yields $R(\tau_{\mathrm{Ross}} = 2/3) \simeq 1.38 \times 10^{13}$ cm $= 196\ R_{\odot}$. We adopt $R(\tau_{\mathrm{Ross}} = 2/3) = 180\ R_{\odot}$. This radius and $T_{\mathrm{eff}}^{\mathrm{Ross}} = 8600$ K yield a luminosity $L = 1.6 \times 10^{5}\ L_{\odot}$. For this luminosity, evolutionary tracks of Schaller et al. (1992) and (Heger & Langer 2000, considering the effects of rotation and the composition gradient) suggest Deneb's mass lies in the range 20 - 25 $M_{\odot}$. Therefore, surface gravities should lie in the range $\log g(R(\tau_{\mathrm{Ross}} = 2/3)) = 1.2 - 1.4$. A full list of the stellar parameters discussed in this paper are compiled in Table 5.

5. DENEB'S SPECTRAL ENERGY DISTRIBUTION

5.1. *Model Parameters*

The most important input parameters which characterize our model atmospheres (for details see Appendix A) are: a model effective temperature, $T_{\star}$, at a reference radius, $R_{\star}$, the gravity, g, at $R_{\star}$, a terminal velocity, v_{∞}, and beta-law exponent, β, a mass-loss rate, $\dot{M}$, a microturbulent velocity, ξ_t, assumed to be depth independent, and the chemical composition. Each of these parameters may be determined to varying degrees of precision by the data. In this section we therefore conduct sensitivity tests in order to examine how well each parameter is constrained by the observations.

As outlined by Venn (1995a,b), a number of studies find that metal abundances for Galactic, early A-type supergiants are near solar (± 0.2 dex). Nitrogen abundances, while enhanced in A-type supergiants relative to unevolved B-stars, are consistent within the uncertainties with solar abundances, since the sun is metal-rich relative to the nearby B-type stars (see, e.g. Edvardsson et al. 1993). A detailed abundance study of Deneb using LTE plane-parallel model atmospheres was recently published by Albayrak (2000). While we would very much like to understand how the accuracy of these abundance determinations is influenced by the lack of non-LTE, spherical, and expanding atmosphere effects, this is beyond the present scope of this work. In this paper we use solar abundances (Grevesse & Noels 1993) for all models.

TABLE 5
STELLAR PARAMETERS FOR DENEB

Parameter	Symbol	Value	Reference
Measured values			
Uniform-disk angular diameter	θ_{UD}	2.40 ± 0.06 mas	§2.7, eqn. 2
Bolometric flux (reddened)	$\mathcal{F}$	$7.1 \pm 0.4 \times 10^{-6}$ erg cm^{-2} s^{-1}	§4.1
Parallax	π	1.01 ± 0.57 mas	Perryman et al. (1997)
Derived values			
Limb-darkened angular diameter	θ_{LD}	2.76 ± 0.06 mas	§3, eqn. 7
Rosseland mean angular diameter			
interferometric model	θ_{Ross}	2.32 ± 0.06 mas	§3, eqn. 10
SED χ^2 fit	θ_{Ross}	2.35 ± 0.01 mas	§5.2.1
Color Excess			
Barnes-Evans relation	$E(B-V)$	$0.09^{+0.04}_{-0.03}$	§4.1, eqn. 17
SED χ^2 fit	$E(B-V)$	0.06 ± 0.01	§5.2.1
Total/selective extinction	R_V	2.9 ± 0.5	§4.1, eqn. 12
Bolometric flux (unreddened)	$\mathcal{F}_0$	$9.8 \pm 2.3 \times 10^{-6}$ erg cm^{-2} s^{-1}	§4.1
Effective Temperature			
interferometry	$T_{\mathrm{eff}}^{\mathrm{Ross}}$	8600 ± 500 K	§4.1, eqn. 18
SED χ^2 fit	$T_{\mathrm{eff}}^{\mathrm{Ross}}$	8420 ± 100K	§5.2.1, eqn. 22, Fig. 6
Radius	$R(\tau_{\mathrm{Ross}} = 2/3)$	$\simeq 180\ R_{\odot}$	§4.2
Luminosity	L	$\simeq 1.6 \pm 0.4 \times 10^5\ L_{\odot}$	§4.2
Mass	M	~ 20 - $25\ M_{\odot}$	§4.2
Surface gravity			
$R(\tau_{\mathrm{Ross}} = 2/3)$ and M	$\log g(R(\tau_{\mathrm{Ross}} = 2/3))$	$\simeq 1.3$	§4.2
stability, Balmer edge	$\log g(R(\tau_{\mathrm{Ross}} = 2/3))$	1.1 - 1.6	§5.2.2, Table 7
Mass-loss Rate			
SED χ^2 fit	$\dot{M}$	$8 \pm 3 \times 10^{-7}$ M$_{\odot}$ yr^{-1}	§5.2.1
spectral lines	$\dot{M}$	$10^{-7} - 10^{-6}$ M$_{\odot}$ yr^{-1}	§6
Terminal Velocity	v_{∞}	$\simeq 225$ km s^{-1}	§6.1, Fig. 19
Velocity Law Exponent	β	$\simeq 3$	§5.2.2, eqn. A2, Table 7
Microturbulent velocity	ξ_t	$\simeq 15$ km s^{-1}	§5.2.2, Table 7

5.2. *Least-squares Analysis*

To compare quantitatively a set of model spectra to the observed spectrum of Deneb from the UV to the radio, both the model and observed spectra have been binned to 20 Å in the UV and the model spectra have been binned to 50 Å in the optical and near-IR to match the resolution of the spectrophotometry in this region. At longer wavelengths, monochromatic fluxes from model spectra are interpolated at wavelengths corresponding to DIRBE, MSX, ISO, SCUBA, and VLA bands.

The model and the observed SED are compared in each wavelength bin:

$$\chi^2 = \sum_{i=1}^{265} \left(\frac{f^0_\oplus(\lambda_i) - F_{\text{model}}(\lambda_i)\frac{1}{4}\theta_\star^2}{\sigma_{f^0_\oplus}(\lambda_i)} \right)^2 \tag{19}$$

where,

$$f^0_\oplus(\lambda_i) = f_\oplus(\lambda_i) \cdot 10^{0.4\frac{A_{\lambda_i}}{A_V} R_V E(B-V)} \tag{20}$$

is the unreddened flux measured at the earth in wavelength bin i, $\sigma_{f^0_\oplus}(\lambda_i)$ is the 1σ uncertainty in this value. In bin i, the interstellar extinction is A_{λ_i}/A_V and the model flux is $F_{\text{model}}(\lambda_i)$. The angular diameter, $\theta_\star$ in radians, scales the model surface flux (at $R_\star$) to the measured flux.

$$\theta_\star = \theta_{\text{Ross}} \frac{R_\star}{R_{\text{Ross}}} \tag{21}$$

5.2.1. *Constraining $T_\star$ and $\dot{M}$*

A least squares sum was computed for set of 45 models with a range of effective temperatures and mass-loss rates (the $T_\star$, $\dot{M}$ grid is shown in Figure 6b). A combination of parameters $\theta_\star$ (range: 1.5–3.5 mas) and $E(B-V)$ (range: 0.05–0.12 mag) was found which minimized the χ^2 for each model. The models, sorted by χ^2, are listed in Table 6 along with best fitting values for $\theta_\star$ and $E(B-V)$ at each $T_\star$ and $\dot{M}$.

Although the best fit model is a good match to the spectrum (see Figures 7 and 8), the reduced chi-square value, $\tilde{\chi}^2 \simeq 4.4$, is large and the χ^2 test yields a very low probability of agreement between the observed and theoretical distributions indicative of a bad fit. In cases like this Bevington (1969) suggests the use of the F test because: "the statistic χ^2 measures not only the discrepancy between the estimated function [model spectrum] and the parent function [actual spectrum], but also the deviations between the data [observed spectrum] and the parent function [actual spectrum] simultaneously." The F test concentrates on the discrepancy between the model spectrum and actual spectrum. The probability that model n with $F = \chi^2_n/\chi^2_{\min}$ is as good a fit to the data as the best fit model is listed in Table 6. From these probabilities the 1σ and 2σ contours are plotted in Figure 6a. The 1σ region encloses the parameter space $T_\star \simeq 8925 \pm 100$ K and $\dot{M} \simeq 8 \pm 3 \times 10^{-7}$ M$_\odot$ yr^{-1}. This effective temperature range is equivalent to

$$T_{\text{eff}}^{\text{Ross}} \simeq 8420 \pm 100 \text{ K} \tag{22}$$

after scaling from $R_\star$ to $R(\tau_{\text{Ross}} = 2/3)$.

This effective temperature is in good agreement with the interferometric Rosseland fundamental effective temperature from equation 18. The least-squares determination of $T_{\text{eff}}^{\text{Ross}}$ has a smaller random uncertainty because a correction for the interstellar extinction is incorporated into the fitting procedure (with the value for R_V fixed), while the full uncertainties in both R_V (equation 11) and $E(B-V)$ (equation 17) from the Barnes-Evans relation enter into the interferometric value of $T_{\text{eff}}^{\text{Ross}}$. We note that the derived reddening for the best fitting models (Table 6, column 6) yield values, $E(B-V) = 0.06 \pm 0.01$, at the low end of the range of equation 17. This result is consistent with the lower mean least-squares $T_{\text{eff}}^{\text{Ross}}$ relative to the mean interferometric $T_{\text{eff}}^{\text{Ross}}$, since the derived bolometric flux will be lower when a lower interstellar extinction is adopted. In addition, the derived angular diameters for the best fitting models (Table 6, column 5) correspond (via equation 21) to $\theta_{\text{Ross}} = 2.35 \pm 0.01$ mas, which is in good agreement with interferometric value of θ_{Ross} from equation 10. In short, the derived interferometric and spectrophotometric values for $T_{\text{eff}}^{\text{Ross}}$, θ_{Ross}, and $E(B-V)$ are in good agreement.

Figure 6b shows the contours of the χ^2 values from Table 6. Models in the region (8500 K, 2×10^{-8} M$_\odot$ yr^{-1}) poorly fit the observed spectrum because the model UV fluxes are too small, particularly right below the Balmer jump and below 1600 Å, and the model millimeter and radio fluxes are too small by roughly one order of magnitude. Models with much higher mass-loss rates and similar effective temperatures (8500 K, 2×10^{-6} M$_\odot$ yr^{-1}) provide a closer match to the millimeter and radio fluxes, but still come up short, and the model UV fluxes are even smaller. Models in the region (9250 K, 2×10^{-8} M$_\odot$ yr^{-1}) poorly fit the observed spectrum because the model UV fluxes below 1600 Å are too large, and the predicted millimeter and radio fluxes are too small by an order of magnitude. For a given $T_\star$, larger $\dot{M}$ values have two effects on the SED relative to lower $\dot{M}$ values: (1) the UV continuum is suppressed, and (2) the radio continuum is enhanced. The hottest, highest mass-loss rate models explored (eg., 9250 K, 3×10^{-6} M$_\odot$ yr^{-1}) produce millimeter and radio fluxes in excess of those observed, and the model UV continuum, while suppressed relative to lower $\dot{M}$ models, is still too large below 1600 Å. The best fitting models are slightly cooler, to match the UV, and have slightly lower mass-loss rates, to match the millimeter and radio fluxes.

TABLE 6
SED (UV to Radio) Fitting Results[a]

Model		Fit Results			
$T_\star$ (K)	$\dot{M}$ ($M_\odot$ yr^{-1})	χ^2	$P(F$ test)	$\theta_\star$ (mas)	$E(B-V)$
8875	1.00E-06	1.14E+03	5.00E-01	2.10	0.05
9000	1.00E-06	1.17E+03	4.13E-01	2.08	0.06
8875	5.00E-07	1.21E+03	3.18E-01	2.10	0.05
9000	5.00E-07	1.23E+03	2.57E-01	2.08	0.06
8750	3.00E-07	1.24E+03	2.44E-01	2.16	0.05
8875	3.00E-07	1.30E+03	1.44E-01	2.16	0.07
9125	1.00E-06	1.31E+03	1.26E-01	2.08	0.08
9000	2.00E-06	1.32E+03	1.21E-01	2.06	0.05
8875	2.00E-06	1.34E+03	9.28E-02	2.10	0.05
9125	5.00E-07	1.37E+03	7.08E-02	2.10	0.09
8750	1.00E-07	1.38E+03	5.97E-02	2.20	0.06
9000	3.00E-07	1.43E+03	3.22E-02	2.16	0.09
9125	3.00E-07	1.45E+03	2.72E-02	2.10	0.09
9125	2.00E-06	1.45E+03	2.50E-02	2.06	0.07
8750	1.00E-06	1.47E+03	1.99E-02	2.16	0.05
8750	5.00E-08	1.47E+03	1.98E-02	2.26	0.08
8750	3.00E-08	1.49E+03	1.46E-02	2.18	0.05
9000	3.00E-06	1.52E+03	9.91E-03	2.04	0.05
8500	1.00E-07	1.52E+03	9.72E-03	2.28	0.05
9000	2.00E-08	1.54E+03	7.58E-03	2.18	0.09
9250	1.00E-06	1.55E+03	6.71E-03	2.08	0.10
8500	5.00E-08	1.55E+03	6.38E-03	2.28	0.05
8750	2.00E-08	1.57E+03	4.53E-03	2.18	0.05
8750	5.00E-07	1.59E+03	3.53E-03	2.16	0.05
9250	5.00E-07	1.61E+03	2.75E-03	2.10	0.11
9000	1.00E-07	1.62E+03	2.23E-03	2.20	0.10
9000	3.00E-08	1.63E+03	1.89E-03	2.20	0.10
9125	3.00E-06	1.64E+03	1.65E-03	2.02	0.06
8750	2.00E-06	1.64E+03	1.65E-03	2.14	0.05
8875	3.00E-06	1.65E+03	1.32E-03	2.10	0.05
9250	2.00E-06	1.67E+03	9.48E-04	2.06	0.09
9250	3.00E-07	1.70E+03	6.61E-04	2.10	0.11
9000	5.00E-08	1.72E+03	4.52E-04	2.22	0.11
9250	3.00E-06	1.86E+03	3.70E-05	2.00	0.07
8500	3.00E-07	1.90E+03	1.74E-05	2.28	0.05
8500	5.00E-07	1.95E+03	8.16E-06	2.26	0.05
8500	3.00E-08	2.00E+03	2.98E-06	2.30	0.05
8750	3.00E-06	2.17E+03	1.19E-07	2.12	0.05
9250	1.00E-07	2.69E+03	0.00	2.14	0.12
9250	2.00E-08	2.71E+03	0.00	2.14	0.12
9250	3.00E-08	2.81E+03	0.00	2.14	0.12
8500	3.00E-06	2.93E+03	0.00	2.22	0.05
8500	2.00E-06	2.94E+03	0.00	2.22	0.05
9250	5.00E-08	3.11E+03	0.00	2.12	0.12
8500	1.00E-06	3.25E+03	0.00	2.24	0.05
8500	2.00E-08	3.36E+03	0.00	2.28	0.05

[a]Columns (1-2): With the exception of parameters $T_\star$ and $\dot{M}$, all models listed share these parameters: $R_\star = 1.2\times10^{13}$ cm, $\log g(R_\star) = 1.3$, $\xi = 15$ km s^{-1}, v_∞ = 225 km s^{-1}, $\beta = 3.0$. Column (3): χ^2 values are from equation (19) for 265 wavelength bins from 1220 Å to 3.6 cm. Column (4): The probability from the F test that the χ^2 value for each model is statistically equivalent to the best fit model. Column (5): The best fit angular diameter value for each $T_\star$, $\dot{M}$ combination. Column (6): The best fit color excess for each $T_\star$, $\dot{M}$ combination. R_V=2.9 is fixed.
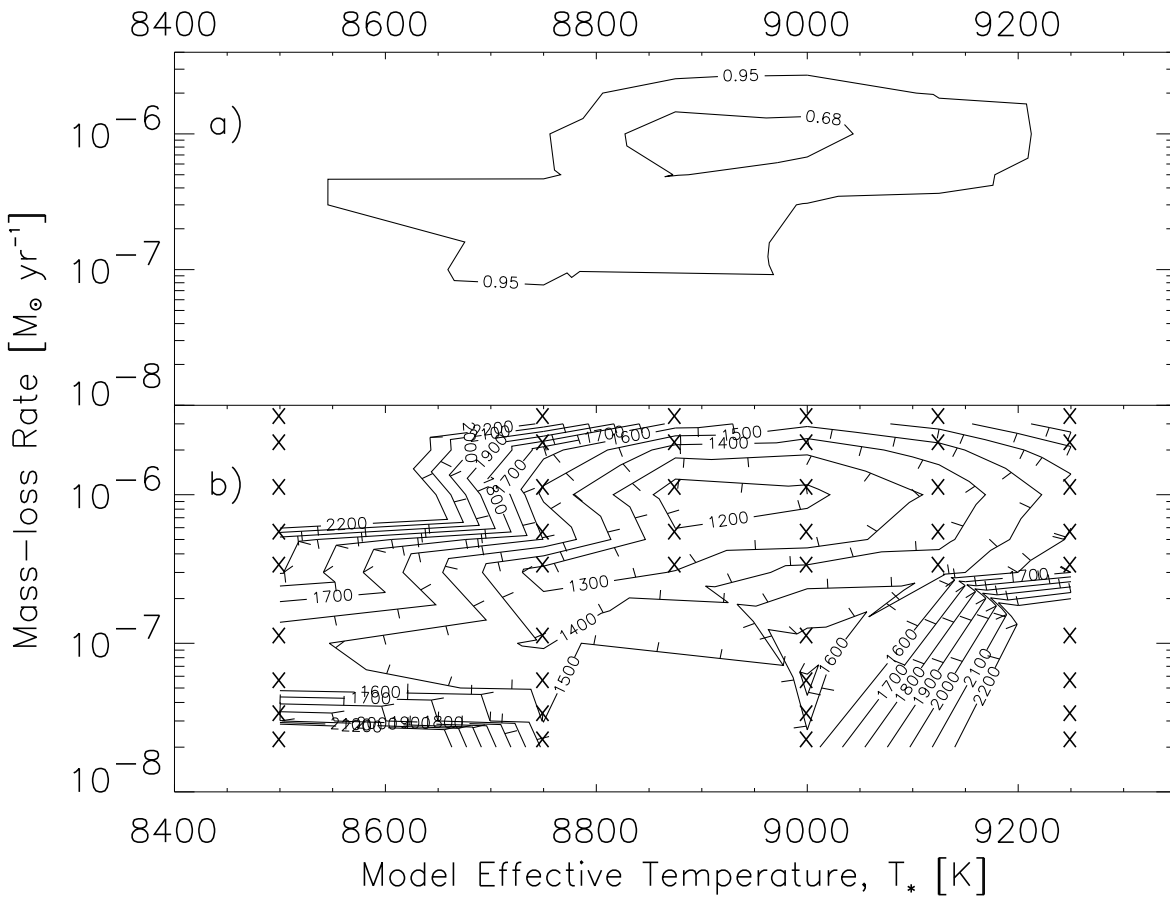
FIG. 6.— (a) Regions (1σ and 2σ) in the ($T_\star$, $\dot{M}$) parameter plane containing the best fit model parameters to the observed spectral energy distribution (SED) of Deneb. The probabilities are listed in Table 6. (b) Contour map of χ^2 in the ($T_\star$, $\dot{M}$) plane of the model fits to the observed SED. The grid of model locations in the parameter plane is marked by x.

$T_* = 8875$ K
$\dot{M} = 1.00e{-}06$ $M_\odot$ yr^{-1}
$\theta_* = 2.08$ mas
$E(B{-}V) = 0.05$
$R_V = 2.4$
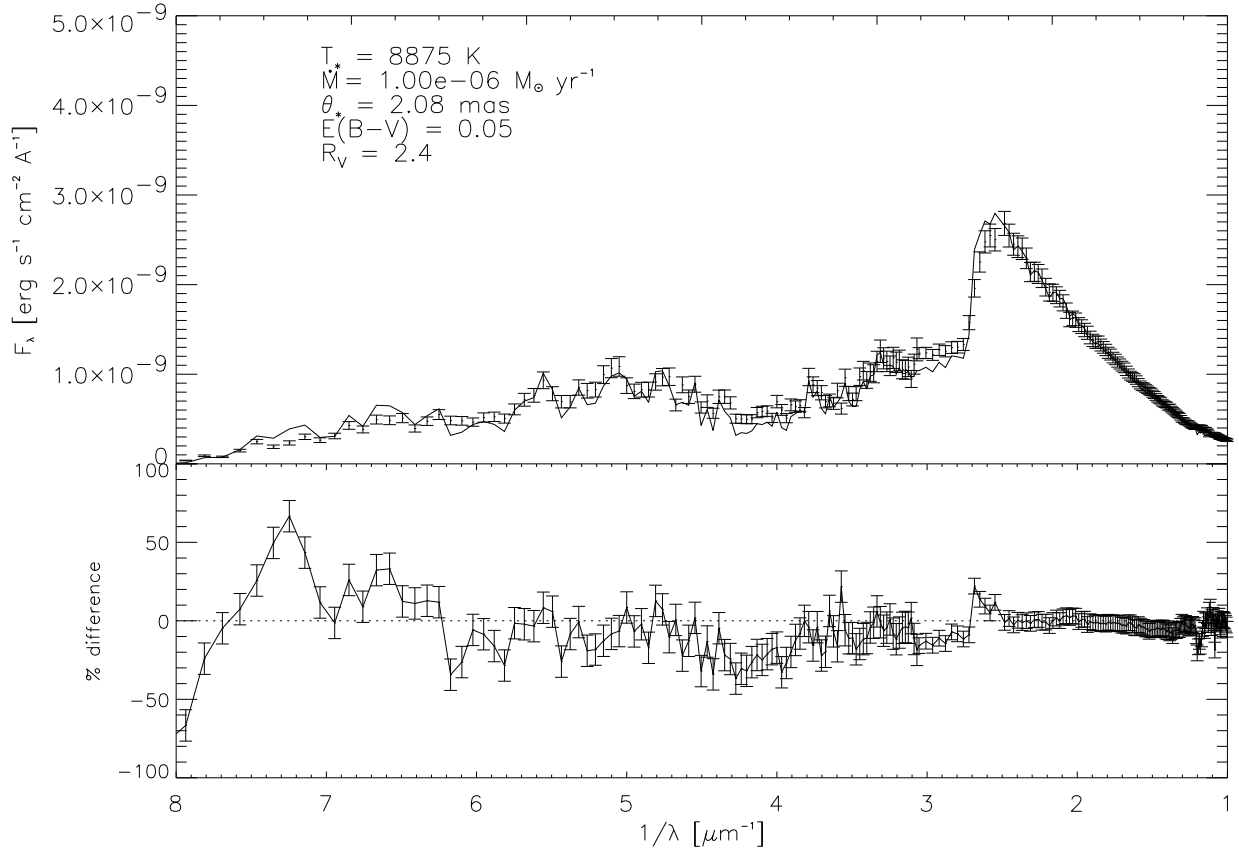
FIG. 7.— Top Panel: Best least squares fit (solid line) to the UV to radio spectrum compared to the UV-optical spectrum of Deneb (error bars), which is binned to 20 Å in the UV and to 50 Å in the optical. The model has been scaled with the angular diameter θ_* (see text) and the data have been corrected for interstellar extinction using the reddening parameters shown. $T_* = 8875$ K is equivalent to $T_{\mathrm{eff}}^{\mathrm{Ross}} = 8370$ K. Bottom Panel: Percentage difference, (model - data)/data, plotted as a function of wavenumber.
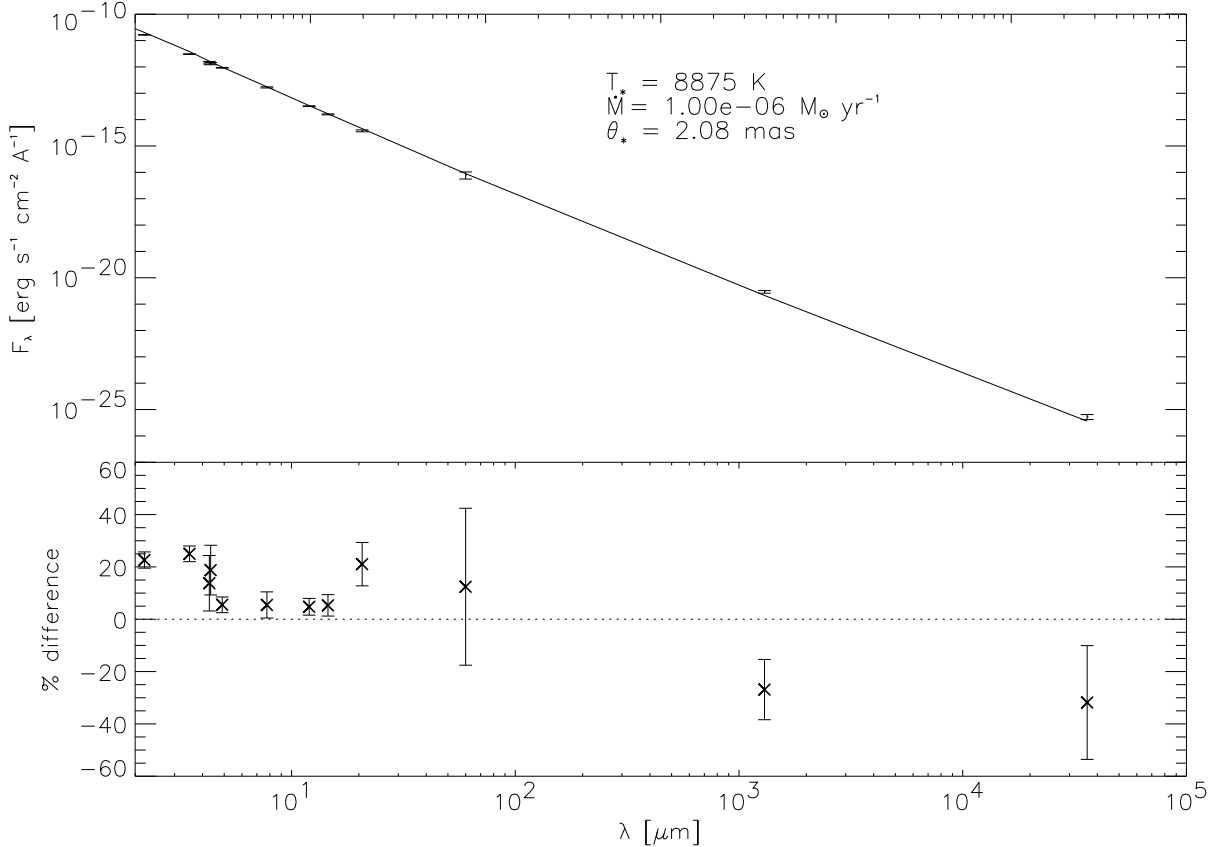
FIG. 8.— Top Panel: Best least squares fit (solid line) to the UV to radio spectrum compared to IR, mm, radio spectrum of Deneb (error bars) from Table 1. The model has been scaled with the angular diameter $\theta_\star$. $T_\star = 8875$ K is equivalent to $T_{\mathrm{eff}}^{\mathrm{Ross}} = 8370$ K. Bottom Panel: Percentage difference, (model - data)/data, plotted as a function of wavelength.

5.2.2. *Constraining Other Parameters*

Our preliminary fits to Deneb's SED revealed that model parameters $T_\star$ and $\dot{M}$ have the largest effects on the model SED. As a result, the parameters $R_\star$, $\log g$, v_∞, β, and ξ_t were fixed in the analysis discussed above. The most straightforward parameter to constrain is the terminal velocity. We find $v_\infty \simeq 225$ km s^{-1} by fitting the blue edge of the Mg II h resonance line profile (see Figure 19). Parameters β, ξ_t, and $\log g$ can be constrained with reference to least squares fits to the observed SED (see Table 7). Parameters β and ξ_t are constrained due to their significant effect on the ultraviolet SED (see Figure 9). Despite the uncertainty in the reddening, β values 2.0 and 4.0 can be rejected with confidence. Similarly, a low microturbulence, $\xi_t = 5$ km s^{-1}, can be rejected.

We find that adjusting the model radius $R_\star$ by $\pm25\%$ has no significant effect on the model SED. However, as shown below in §6.2, the radius can affect synthetic P-Cygni profiles because, via the continuity equation (A1), the parameter $R_\star$, for a fixed mass-loss rate, sets the gas density at the base of the wind.

The model with $\log g(R_\star) = 1.7$ can be rejected at the 3σ level due to this parameter's strong effect on the Balmer jump. From the requirement of the hydrostatic equilibrium (equations A7, A8, and A9) in the deepest layers ($\tau_{\rm Ross} \simeq 100$) of the model atmosphere we can assign a lower limit of to the gravity of $\log g(R_\star) \geq 1.2$. Models with lower values of $\log g(R_\star)$ fail to have positive effective gravities in the deepest layers of the atmosphere, thus making a hydrostatic solution impossible. The radiative acceleration is quite significant in the hydrostatic layers. For example, in the $\log g(R_\star) = 1.7$ model the effective gravity, $\log g_{\rm eff}$, drops as low as 1.43 in the hydrostatic layers, while for the $\log g(R_\star) = 1.3$ model, the minimum $\log g_{\rm eff}$ is 0.4. The surface gravity constraint is then $1.2 \leq \log g(R_\star) \leq 1.7$. This range of values can be scaled to the reference depth $R(\tau_{\rm Ross} = 2/3)$ via

$$\log g(R(\tau_{\rm Ross} = 2/3)) = \log g(R_\star) + 2\log\left(R_\star/R(\tau_{\rm Ross} = 2/3)\right) \qquad (23)$$

yielding $1.1 \leq \log g(R(\tau_{\rm Ross} = 2/3)) \leq 1.6$ for the same ratio of of radii (0.89) as equation 9.

5.3. *Deneb's Continuum Beyond 1 μm*

Figure 10 shows the IR, millimeter, and radio observations from Table 1 compared with the synthetic continua from a set of $T_\star = 9000$ K models listed in Table 6. The synthetic continua are scaled with $\theta_\star = 2.08$ mas, consistent with the NPOI diameter. Models with mass-loss rates $\dot{M} \gtrsim 3 \times 10^{-6}$ M$_\odot$ yr^{-1} can be ruled out by the 3σ upper limit at 870 μm from the HHT. Except for the DIRBE band 1A, observations at shorter wavelengths are consistent with this. The detections at 1.35 mm and 3.6 cm, with SCUBA and the VLA respectively, rule out models with mass-loss rates $\dot{M} \lesssim 5 \times 10^{-7}$ M$_\odot$ yr^{-1}. These results are consistent with the least squares results from the full UV to radio spectrum.

The synthetic continua shown in Figure 10 were computed from spherical expanding atmosphere models whose temperature structures are consistent with radiative equilibrium and where non-LTE line-blanketing has been self-consistently included. This is important because at wavelengths beyond 1 mm the synthetic continua are quite sensitive to the degree of line-blanketing employed in the construction of the model atmosphere. This is illustrated in Figure 11, which shows the results of a test where five wind models, which differ in the degree of line-blanketing, but have otherwise identical parameters, were computed. As easily seen with reference to the hydrostatic model spectrum, the expanding atmosphere spectra predict significantly larger fluxes. The effects of line-blanketing and non-LTE are no less significant. For example, at 3 cm, the continuum opacity wind model produces ∼10 times more flux than our most sophisticated non-LTE line-blanketed wind model, and the LTE line-blanketed wind model produces ∼1/2 as much flux. The LTE continuum-only model spectrum shows a turnover at ∼ 30 cm due to truncation at the outer boundary of the model, 200 $R_\star$. A similar model with an other boundary of 400 $R_\star$ does not show a turnover. The line-blanketed wind models, which are not fully ionized to the outer boundary, are not sensitive to this truncation.

There are two important factors at play here. First, the incorporation of metal line-blanketing in the radiative equilibrium solution cools the outermost layers of the atmosphere (classic surface cooling), especially at depths where the radio continuum forms. In LTE, lower electron temperatures mean lower ionization, and therefore less thermal radio emission

TABLE 7

LEAST SQUARES RESULTS FOR PARAMETERS $R_\star$, $\log g$, β, ξ_t[a]

Model				Fit Results			
$\log g(R_\star)$	$R_\star$	β	ξ_t	χ^2	$P(F$ test$)$	$\theta_\star$	$E(B-V)$
1.3	1.50e+13	3.0	15	1.15e+03	5.00e-01	2.080	0.060
1.3	1.20e+13	3.0	15	1.17e+03	4.32e-01	2.080	0.060
1.3	9.00e+12	3.0	15	1.26e+03	2.25e-01	2.080	0.060
1.3	1.20e+13	3.0	25	1.31e+03	1.36e-01	2.060	0.050
1.5	1.20e+13	3.0	15	1.46e+03	2.66e-02	2.060	0.050
1.3	1.20e+13	2.0	15	1.69e+03	8.17e-04	2.260	0.120
1.7	1.20e+13	3.0	15	1.87e+03	3.63e-05	2.040	0.050
1.3	1.20e+13	3.0	5	2.13e+03	2.98e-07	2.120	0.090
1.3	1.20e+13	4.0	15	2.23e+03	5.96e-08	2.020	0.050

[a]Columns (1-4): The models listed here have the fixed values $T_\star = 9000$ K and $\dot{M} = 10^{-6}$ M$_\odot$ yr^{-1}. Columns (5-8) as described in Table 6.
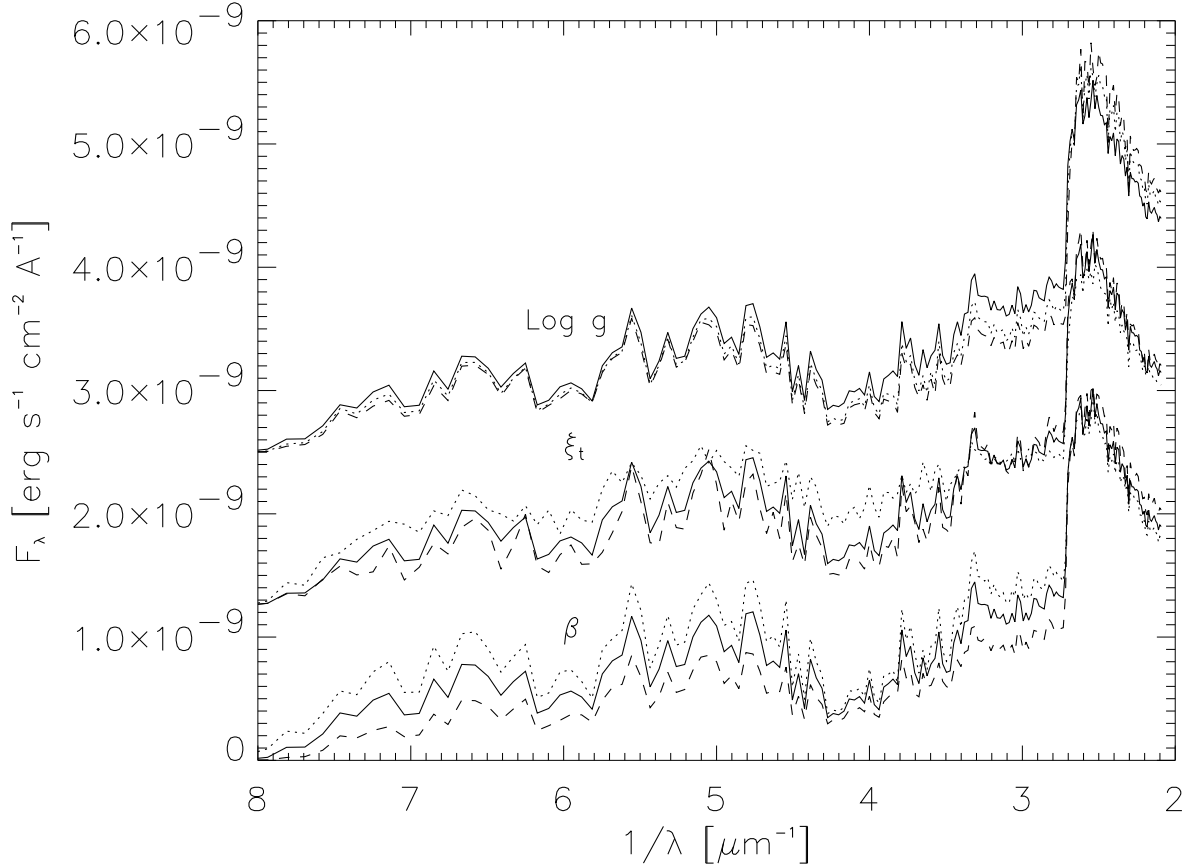
FIG. 9.— Synthetic UV continua from three sets (from top to bottom) of three models: surface gravity, $\log g = 1.3$ (solid), 1.5 (dotted), 1.7 (dashed); the microturbulent velocity, $\xi_t = 5$ km s^{-1}(dotted), 15 km s^{-1}(solid), 25 km s^{-1}(dashed); and the velocity law exponent, $\beta = 2.0$ (dotted), 3.0 (solid), 4.0 (dashed). These synthetic spectra have been binned to 20 Å resolution to show the gross features of the spectrum. All models have the following parameters, unless otherwise noted: $T_\star = 9000$ K , $\log g(R_\star) = 1.3$, $\dot{M} = 10^{-6}$ M$_\odot$ yr^{-1}, $\beta = 3.0$, $\xi_t = 15$ km s^{-1}. All models have been scaled by $\theta_\star = 2.08$ mas. Constants of 1.25×10^{-9} and 2.5×10^{-9} erg s^{-1} cm^{-2} Å^{-1} have been added to the top two sets of models for clarity. The effects of $\log g$ can be seen on both sides of the Balmer discontinuity. The effects of varying ξ_t from 5 to 25 km s^{-1} are apparent below 3000 Å (> 3.5 μm^{-1}) where the flux drops by roughly a factor of two. The effects of varying β from 2.0 to 4.0 are significant below the Balmer jump where the flux drops by roughly 50%.
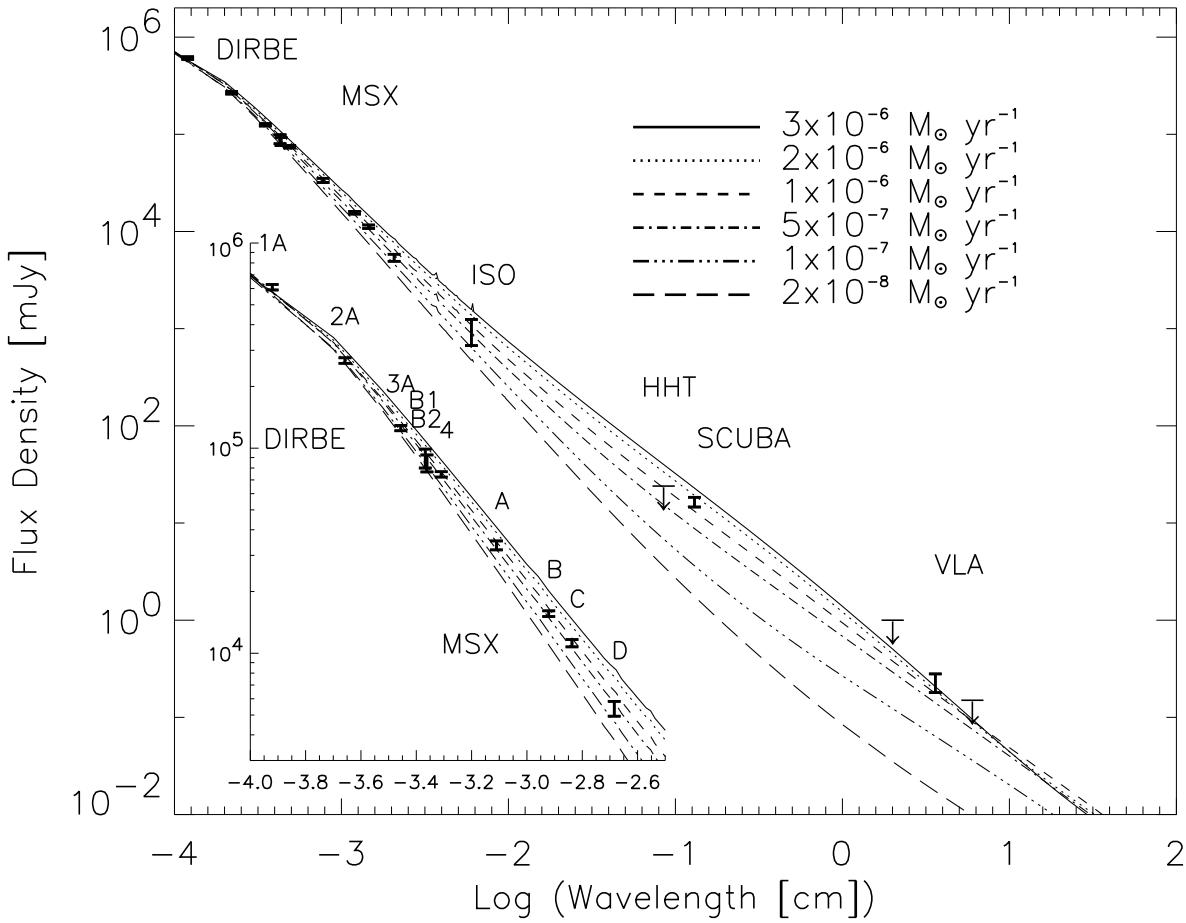
FIG. 10.— Infrared, millimeter and radio photometry of Deneb from Table 1. Synthetic continua for models listed in Table 6 with $T_\star =$ 9000 K and 6 different mass-loss rates are shown for comparison. The inset shows a close up of the COBE/DIRBE and MSX photometry.
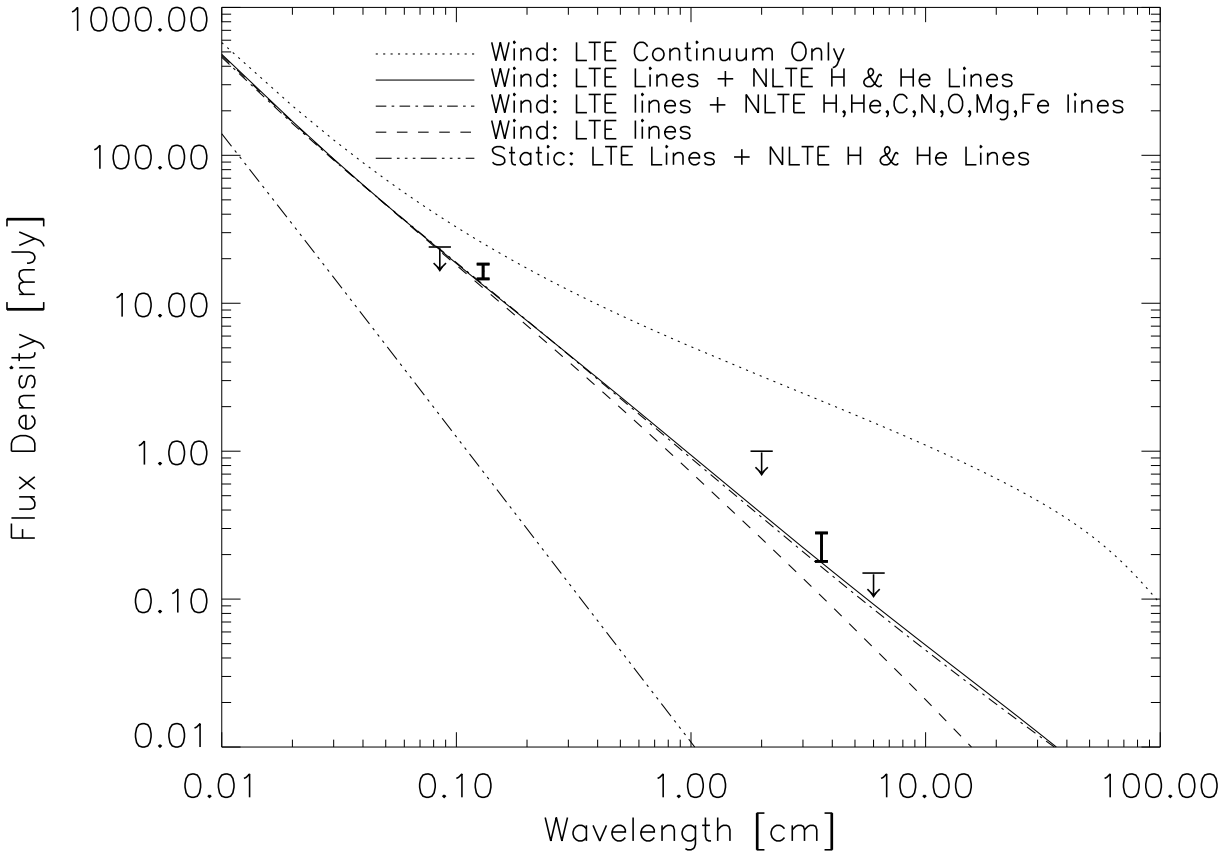
FIG. 11.— Comparison of 4 wind models with identical parameters ($T_\star = 9000$ K, $T_{\text{eff}}^{Ross} = 8600$ K, $\dot{M} = 10^{-6}$ $M_\odot$ yr^{-1}, $R_\star = 1.2$e13 cm, $\log g(R_\star) = 1.3$, $\xi = 15$ km s^{-1}, $v_\infty = 225$ km s^{-1}, $\beta = 3.0$), showing the importance of line-blanketing on the predicted radio flux. A hydrostatic model ($T_\star = 8600$ K, $R_\star = 1.2$e13 cm, $\log g(R_\star) = 1.3$, $\xi = 15$ km s^{-1}) is shown for reference. These synthetic spectra have been scaled with $\theta_\star = 2.08$ mas. The HHT, SCUBA, and VLA data are shown for comparison.

is expected in the presence of line-blanketing relative to the continuum-only opacity case. Second, photoionization is enhanced in non-LTE. Non-LTE photoionization affects the ionization state of the outer layers because they are radiatively coupled to the hotter radiation field at depth. In non-LTE, the ionization fraction in the outermost layers is enhanced relative to the LTE line-blanketed case, which leads to more thermal radio emission.

The sensitivity of the radio continuum to the degree of ionization in the extended stellar envelope makes it clear that the application of a fully ionized, uniform, spherically symmetric mass flow model commonly employed in mass-loss rate estimates for O- and B-type supergiants (Scuderi et al. 1998; Drake & Linsky 1989) won't work for A-type supergiants. Furthermore, in such models the radio spectrum follows the power-law $S_\nu \propto \nu^{2/3}$, but Deneb exhibits a spectral slope between 1.35 mm and 3.6 cm consistent with $S_\nu \propto \nu^{1.26\pm0.01}$, and is therefore inconsistent with a fully ionized wind. Simon et al. (1983) studied thermal radio emission from partially ionized circumstellar environments and winds. They found that the slope of radio spectrum varies from the fully ionized, optically thin case, $(S_\nu \propto \nu^{0.6})$, to the optically thick, Rayleigh-Jeans case, $(S_\nu \propto \nu^2)$. Deneb is an intermediate case. The steepness of a radio spectrum depends on the degree of ionization and radial extent of the ionized envelope. We find the same result, where the degree of ionization is controlled by line cooling and photoionization. The optically thick case is represented by a geometrically thin, hydrostatic model (see Figure 11).

As demonstrated above, for a given effective temperature, the degree of line-blanketing, photoionization, and the mass-loss rate have the largest effects on the synthetic spectrum beyond 1 μm. The synthetic spectrum is also affected to a much smaller degree by other model parameters. Figure 12 shows the sensitivity of the synthetic spectrum, relative to a good fitting reference model, to changes in β, $T_\star$, $R_\star$, ξ_t, and $\log g$. Changing each of these parameters has systematic effects on the synthetic radio continua. Higher (lower) model temperatures increase (decrease) the ionization in the wind and produce higher (lower) fluxes. Changing $T_\star$ by 250 K has little effect below 1 mm. Larger (smaller) values of $R_\star$ yield lower (higher) wind densities for a fixed mass-loss rate and as a result yields slightly lower (higher) fluxes. Higher $\log g$ values yield slightly lower fluxes and varying ξ_t has no significant effect on the fluxes.
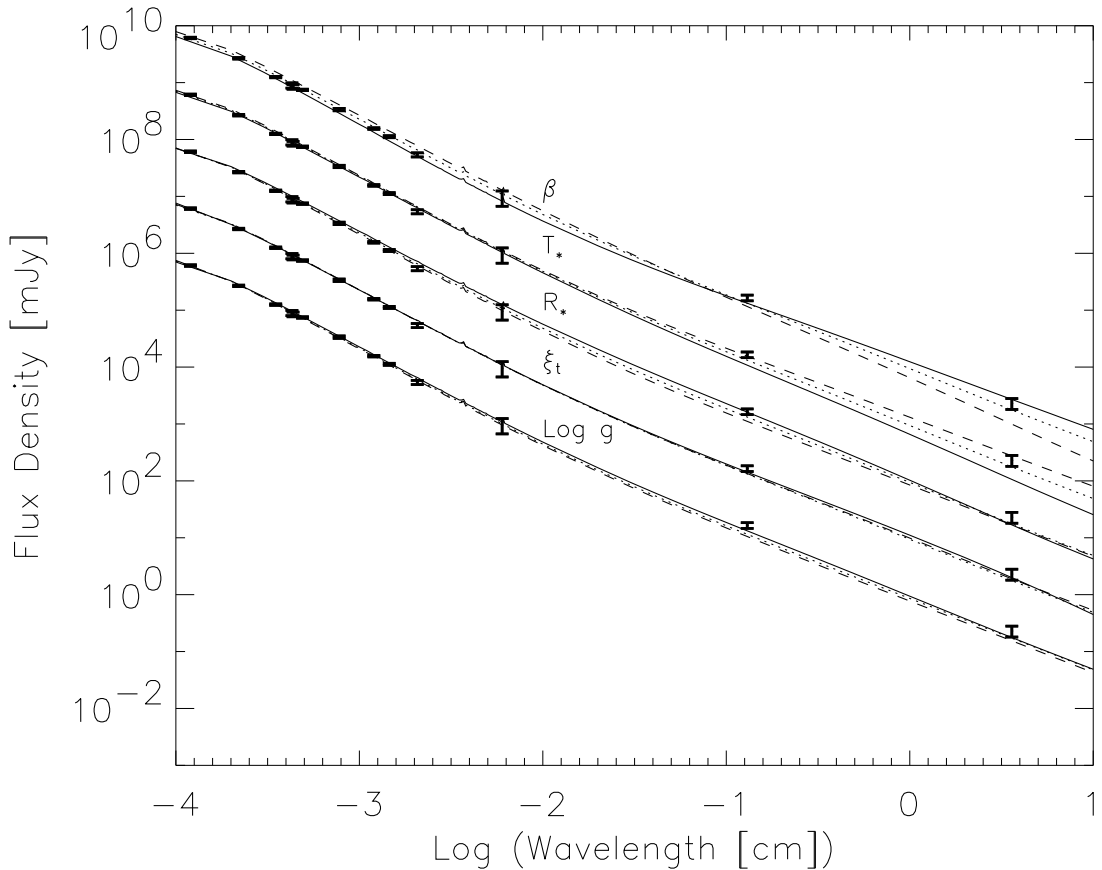
FIG. 12.— Synthetic IR, millimeter, radio continua from five sets (from top to bottom): the velocity law exponent, $\beta = 2.0$ (dotted), 3.0 (solid), 4.0 (dashed); the model temperature, $T_\star = 8750$ K (dotted), 9000 K (solid), 9250 K (dashed); the model radius, $R_\star = 130$ $R_\odot$ (dotted), 172 $R_\odot$ (solid), 215 $R_\odot$ (dashed); microturbulence, $\xi_t = 5$ km s^{-1}, 15 km s^{-1}, 25 km s^{-1}; and the surface gravity, $\log g = 1.3$ (solid), 1.5 (dotted), 1.7 (dashed). All models have the following parameters, unless noted otherwise: $T_\star = 9000$ K , $\log g(R_\star) = 1.3$, $\dot{M} = 10^{-6}$ M$_\odot$ yr^{-1}, $\beta = 3.0$, $\xi_t = 15$ km s^{-1}. The models are scaled using $\theta_\star = 2.08$ mas. Each set of three models is offset by a factor of 10 for clarity. The DIRBE, MSX, ISO, SCUBA, and VLA data are shown for comparison.

The velocity law parameter, β, has a very interesting effect on the synthetic fluxes. At wavelengths beyond 0.5 mm, larger values of β result in lower fluxes, while shortward of 0.5 mm the opposite is true. This behavior in the synthetic radio spectra is a result of the run of electron pressure with depth in the wind as a function of β. At shorter wavelengths, where the opacity is lower, the continuum forms in the inner wind ($\sim 3R_\star$) where the gas and electron densities are regulated primarily by the velocity law through the continuity equation. As a result, models with larger β values have higher densities at this depth and thus higher fluxes. Further out in the wind ($\sim 10R_\star$), where the 3 cm continuum forms, non-LTE effects are more important and the situation is reversed. At these depths the electron temperature and gas density structures are essentially identical for all β values, but the electron densities are higher for models with the smaller β values. This happens because the models with smaller β values have warmer temperature structures at depth (see, for example, the Balmer continuum as a function of β in Figure 9) and the resulting radiation field from these layers ionizes the wind more substantially than models with larger β values. For example, the $\beta = 2.0$ model has the majority of hydrogen ionized out to a radius of $R = 1640\ R_\odot$, while for the $\beta = 4.0$ model, the majority of hydrogren is ionized out to only $R = 610\ R_\odot$.

In summary, of all the model parameters, $\dot{M}$ has the largest effect on the synthetic continuum beyond 1 μm. Non-LTE photoionization, high $T_\star$ values, and small β values all increase model fluxes at centimeter wavelengths for a fixed $\dot{M}$.

6. DENEB'S LINE SPECTRUM

6.1. *The Ultraviolet Line Spectrum*

Deneb's rich UV line spectrum, with its multitude of iron peak absorption lines, is a good diagnostic for the column density in the expanding atmosphere and therefore should be a good diagnostic for the mass-loss rate. Modeling the detailed UV spectrum provides an independent mass-loss rate estimate from that of the IR, mm, radio continuum because the latter is based on the integrated emissivity of the extended atmosphere, while the former is based on the line-of-sight column density toward the stellar photosphere.

Let us examine a portion of an *IUE* spectrum relative to a hydrostatic model synthetic spectrum. Figure 13 shows that the synthetic spectrum reproduces the overall appearance of the observed spectrum quite well. However, in the observed spectrum the stronger lines are considerably less saturated, broader, and blended relative to the model spectrum. This is almost certainly due to these lines forming in the wind and sampling its velocity field, as has been noted by others (e.g. Praderie et al. 1980). The 1640 Å to 1670 Å region is chosen because here the synthetic spectra are quite sensitive to the value of $\dot{M}$ and this spectral region is dominated by Fe II absorption lines. In all comparisons to the *IUE* data, the models are scaled with an angular diameter of $\theta_\star = 2.08$ mas and the data have been corrected for interstellar extinction (curve for HD 199579, $E(B-V) = 0.06$, $R_V = 2.9$).

Now we examine the synthetic UV spectra from the same models we compared to the data beyond 1 μm (see Figure 10). Figure 14 shows a comparison of six synthetic spectra with LTE metal-line blanketing and mass-loss rates from 2×10^{-8} $M_\odot$ yr^{-1} to 3×10^{-6} $M_\odot$ yr^{-1} to the *IUE* spectrum SWP 10375. The lowest mass-loss rate model, $\dot{M} = 2 \times 10^{-8}$ $M_\odot$ yr^{-1}, appears to be most consistent with the windows of low opacity in the observed spectrum: 1645 Å, 1656 Å, 1660 Å, and 1662 Å. Spectra from these LTE models with higher mass-loss rates (higher wind column densities) show a very distorted spectrum, inconsistent with the observations. In these higher $\dot{M}$ models, the line spectrum forms at larger radii, where the velocity field distorts and washes out the spectrum. However, even the $\dot{M} = 2 \times 10^{-8}$ $M_\odot$ yr^{-1} model cannot provide as good a match to the observed spectrum as the hydrostatic model (see Figure 13). These results are very much at odds with the IR, mm, radio continuum anaylsis which indicates $\dot{M} > 10^{-7}$ $M_\odot$ yr^{-1}.

A solution to this inconsistency between the radio and UV mass-loss rate estimates is to use a model which treats Fe I-III in non-LTE (see §A.1 for details on the construction of the model ions and the atomic data). This is critically important. Figure 15 shows that the temperature structures for the LTE and non-LTE Fe I-III models are quite similiar, as expected since the synthetic radio spectra from the two models are in close agreement (see Figure 11). However, Figure 16 shows the dramatic non-LTE effect of the radiation field on the ionization structure of Fe in the wind: Fe$^+$ is ionized to Fe^{++}, significantly dropping the Fe$^+$ column density in the wind relative to the LTE case. Most of the strong Fe II transitions between 1640 Å and 1670 Å have lower levels between 0.2 eV and 1 eV above the ground state, in terms a^{4}F and a^{4}D. These levels are seriously under-populated relative to LTE as shown in Figure 17. The resultant non-LTE synthetic spectrum (Figure 18) is a much improved match to the observed spectrum with a mass-loss rate consistent with the radio continuum result.

The bottom panel of Figure 18 shows the comparison of the non-LTE model spectrum and the *IUE* data. The overall match to the 1640 Å to 1670 Å region is generally good, but several strong lines do not appear in the model spectrum: e.g., 1645.015 Å, 1648.403 Å, and 1667.913 Å. These lines do appear in the hydrostatic model (see Figure 13) and are therefore in the LTE line list (Kurucz & Bell 1995), but are missing or very weak in the non-LTE spectrum. Specifically, consulting Kurucz (1994) we find that the 1645.015 Å line (d^7 a^{4}F$_{9/2}$ – (3H)4p z^{2}I$_{11/2}$) is missing from the synthetic spectrum because the upper level (62662 cm^{-1}) is missing from the model atom. The 1648.403 Å line ((5D)4s a^{6}D$_{5/2}$ – (3P)4p y^{4}P$_{3/2}$) is an intercombination line in LS-coupling, and its predicted gf-value falls below the $\log(gf) > -3.0$ cutoff for our Fe II model atom. The data suggest the true gf-value is larger, which is not surprising given the large uncertaintly likely for a theoretical gf-value from a spin-forbidden transition. The 1667.913 Å line (d^7 a^{2}P$_{1/2}$ – (1D)4p w^{2}P$_{1/2}$) by comparison has a more highly excited lower level (18882.702 cm^{-1} versus 1872 cm^{-1} to 8846 cm^{-1} for the a^{4}F
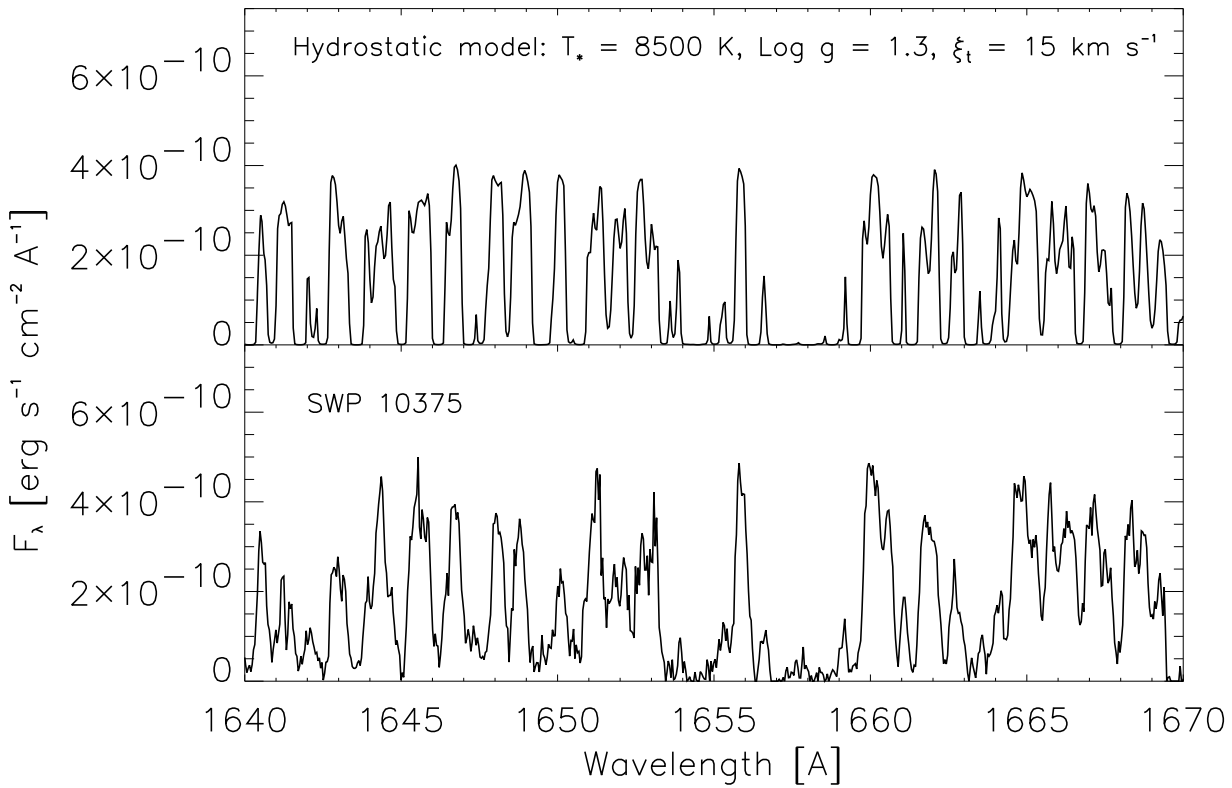
FIG. 13.— Section of the high-dispersion *IUE* spectrum SWP 10375 (bottom panel) compared with a synthetic spectrum (top panel) from a hydrostatic model. There is good correspondance between the strong absorption features in the model and the data, however the synthetic line profiles are much too saturated relative to the observed spectrum. The velocity field present in Deneb's atmosphere desaturates and blends the strong absorption lines.
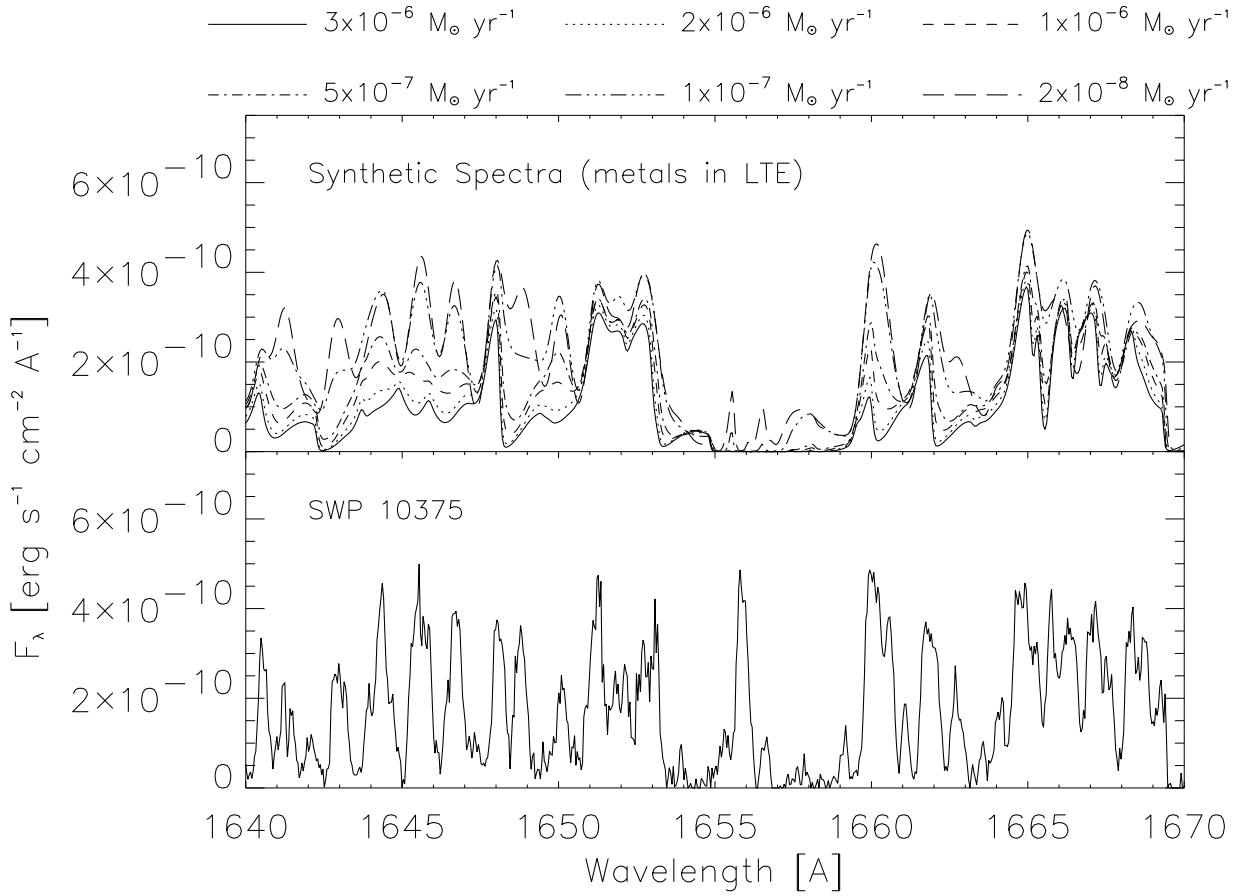
FIG. 14.— Section of the high-dispersion *IUE* spectrum SWP 10375 (bottom panel) compared to a set of synthetic spectra (top panel) from models with different mass-loss rates. This spectral region is dominated by Fe II lines, however in these models all species except H I and He I-II are treated in LTE.

and a^{4}D terms) and may be quenched by the Boltzmann factor, and possibly by inaccurate radiative and collisional rates. In constrast, the strong lines which are well matched by the synthetic spectrum (e.g., 1643.578 Å, 1650.704 Å, 1663.222 Å) have upper levels with highly pure-LS eigenvectors (weak intermediate coupling) which are expected to yield the most reliable transition strengths. The complexity of the high-dispersion UV spectrum and the limitations of the atomic data do not allow to us to better constrain other model parameters, such as β, from this comparison.

A non-LTE treatment also provides a better fit to the Mg II h and k resonance lines and their satellites as shown in Figure 19. The non-LTE synthetic spectrum more accurately reproduces the observed spectrum relative to the LTE case in two respects: (1) the reduced strength of the h and k P-Cygni emission components and, (2) the lower velocity shifts of the Mg II satellite lines at -450 km s^{-1} and +325 km s^{-1}. As in the case of Fe II, enhanced ionization in the non-LTE case reduces the Mg II column density such that the unsaturated satellite lines form deeper in the wind at lower velocities. The models in Figure 19 are parameterized with $v_\infty = 225$ km s^{-1} (maximum model velocity, $v_{\max} = 222$ km s^{-1}), and provide a good match to the blue edge of the h and k P-Cygni absorption troughs. Because of their strength, the resonance lines probe the highest velocities in the wind and thus fix the v_∞ parameter.

6.2.   *Visual-IR Line Spectrum*

6.2.1.   *The Hα line*

At optical wavelengths, the most conspicuous indicator of mass-loss in early-type supergiants is the P-Cygni character of the Hα line. Like all BA-type supergiants, Deneb's Hα profile is variable (Kaufer et al. 1996). Deneb's Hα profile distinguishes itself from most supergiants in that it lacks broad emission wings normally attributed with electron scattering. Despite being the protype of the class, Deneb's Hα profile has only been modeled in detail twice to our knowledge.

Reasonable fits to several of Deneb's Hα profiles have been achieved by Kunasz & Morrison (1982) and Scuderi et al. (1992). Unfortunately, the model parameters and assumptions used in these works are inconsistent with the present observational data. In the former work, the best fits were achieved by adopting terminal velocities of 120 km s^{-1} and 140
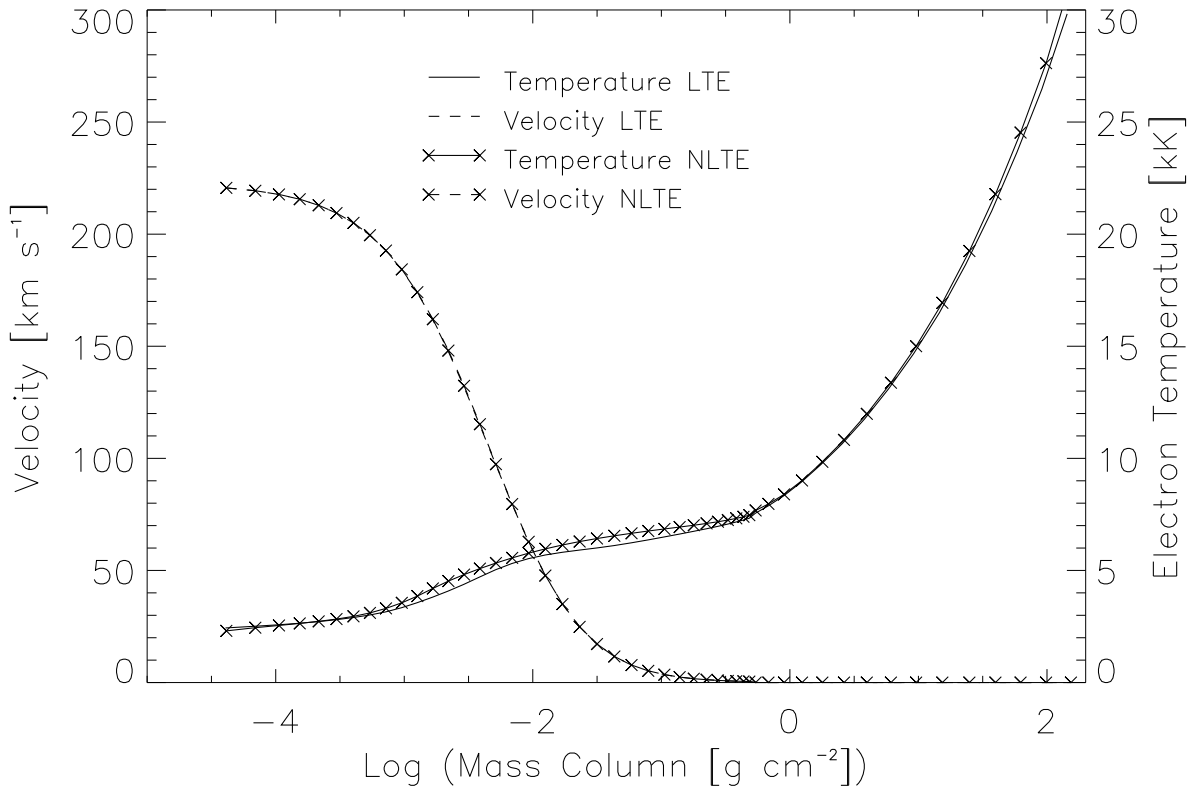
FIG. 15.— Comparison of the velocity (left ordinate) and electron temperature (right ordinate) structures for two models with and without non-LTE metal line-blanketing of species C I-III, N I-III, O I-III, Mg II, Fe I-III. Both models have full LTE line-blanketing for those species not treated in non-LTE. The models have the following parameters: $T_\star = 9000$ K , $\log g(R_\star) = 1.3$, $\dot{M} = 10^{-6}$ M$_\odot$ yr^{-1}, $\beta = 3.0$, $\xi_t = 15$ km s^{-1}. The non-LTE model has a slightly warmer temperature structure from the base of the wind at 10^0 g cm^{-2} to 10^{-3} g cm^{-2} due to photoelectric heating.
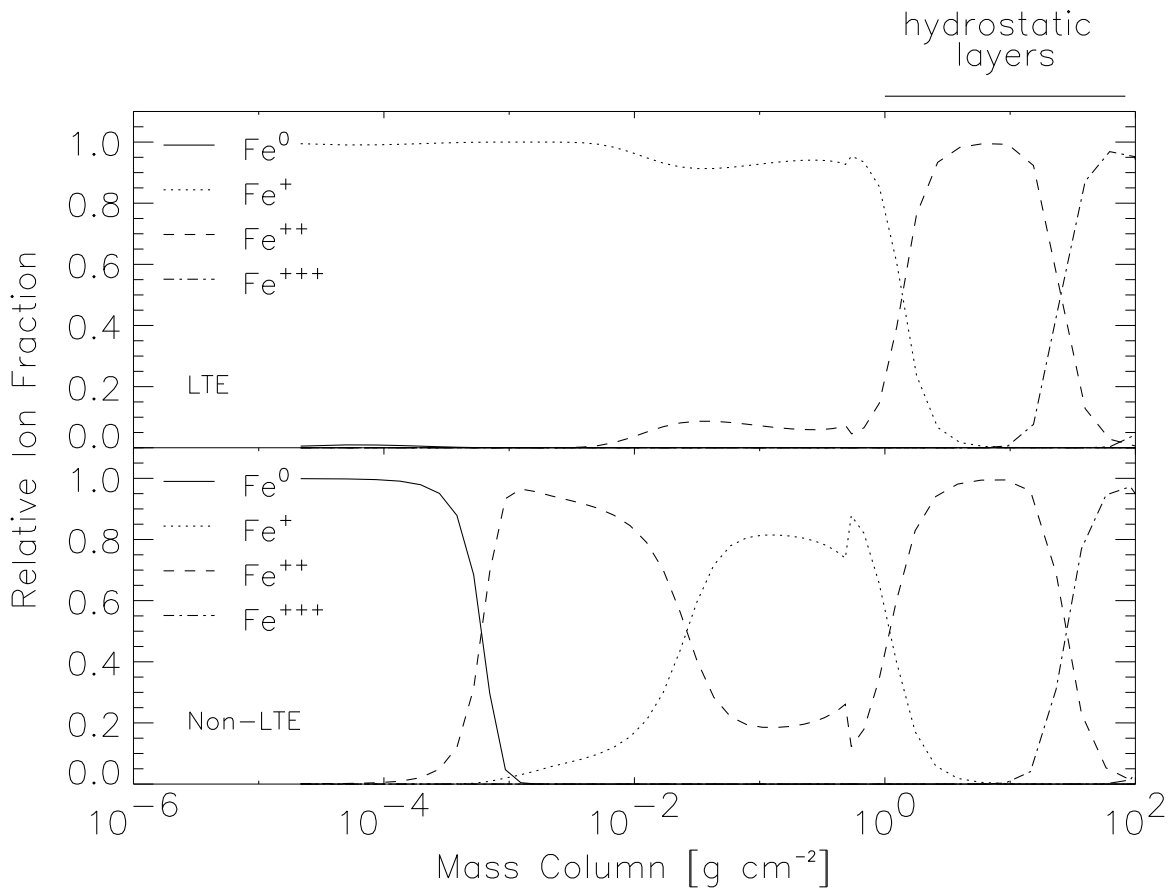
FIG. 16.— Ionization structure of Fe from a model with LTE metal line-blanketing (top) and a model with partial non-LTE metal line-blanketing, including Fe I, Fe II, and Fe III (bottom). A comparison of the two structures shows they are in good agreement in the hydrostatic layers where LTE is a good assumption. Further out in the wind, the two structures differ considerably. The dominant stage of Fe in the wind is Fe^+, when treated in LTE. In non-LTE, Fe^{++} is the dominant stage of Fe throughout most of the wind, rapidly recombining to Fe^0 in the outermost zones. The different ionization structures in the LTE and non-LTE cases lead to significantly different synthetic line spectra in the UV.
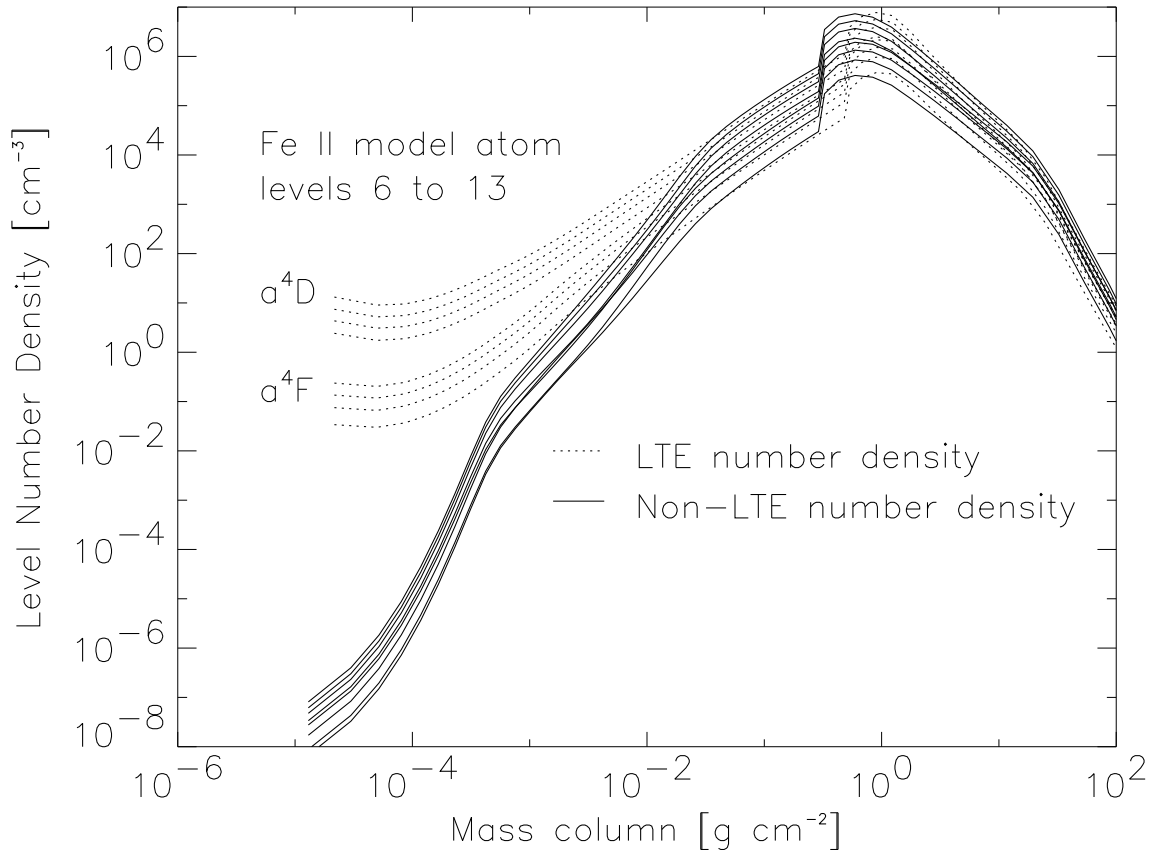
Fig. 17.— Computed number densities for specific Fe II levels from terms a^4F and a^4D as a function of depth in the atmosphere. These levels are the lower levels of transitions which are found in the 1640 Å to 1670 Å spectral region shown in Figures 14 and 18. Level number densities are shown for a model with LTE Fe I-III (dotted-lines) and a model with non-LTE Fe I-III model (solid-lines). At depths greater than than 1 g cm^{-2}, the hydrostatic portion of the atmosphere, the LTE and non-LTE level populations are in close agreement. In the wind, non-LTE level densities are strongly depleted relative to LTE level densities by the effects of the ionizing radiation field.
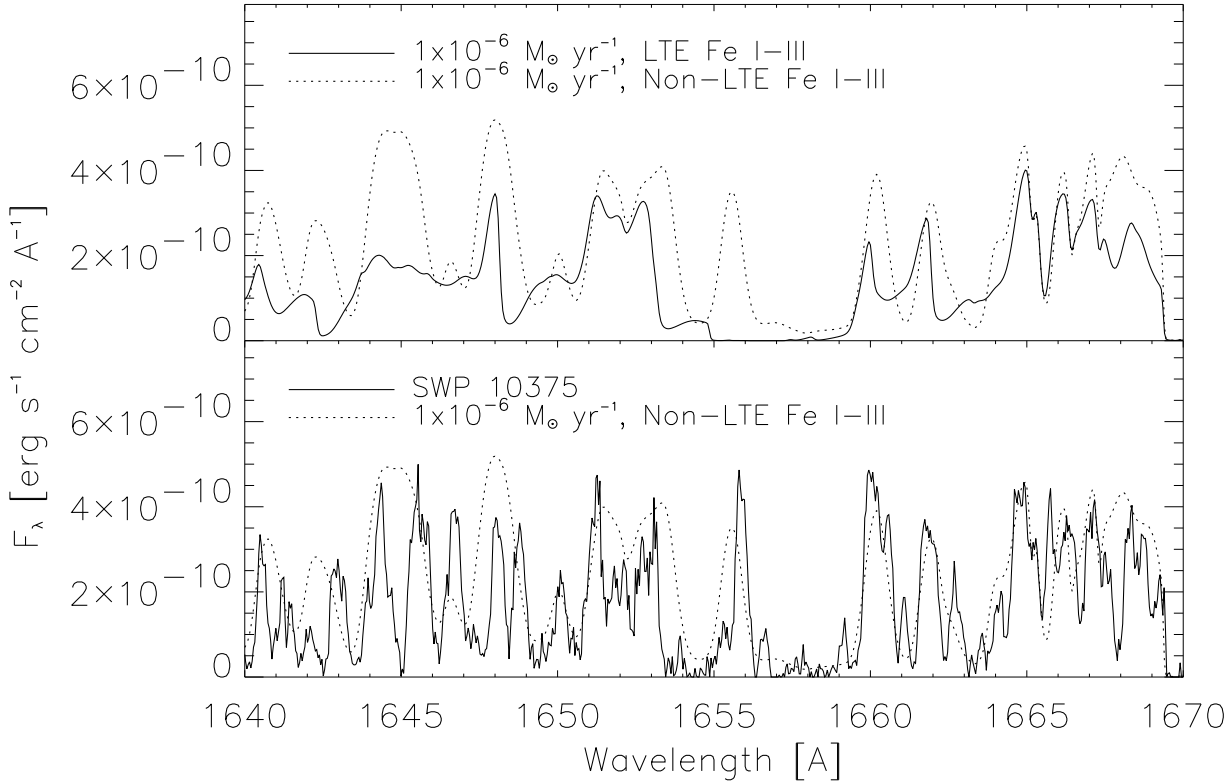
FIG. 18.— (Top) Synthetic spectra from the two models shown in Figure 15. One model has non-LTE Fe I-III line-blanketing, the other does not. The two models have otherwise identical parameters. The reduced Fe II column density in the non-LTE case means the strong Fe II lines probe lower velocities in the wind compared to the LTE case. For example, the two strong aborption features between 1640 Å and 1645 Å are shifted by –93 km s^{-1} in the LTE case relative to the non-LTE case. Most strikingly, the opacity window at 1656 Å is completely missing in the LTE case. (Bottom) Non-LTE synthetic spectrum from the top panel is compared with the *IUE* spectrum SWP 10375.
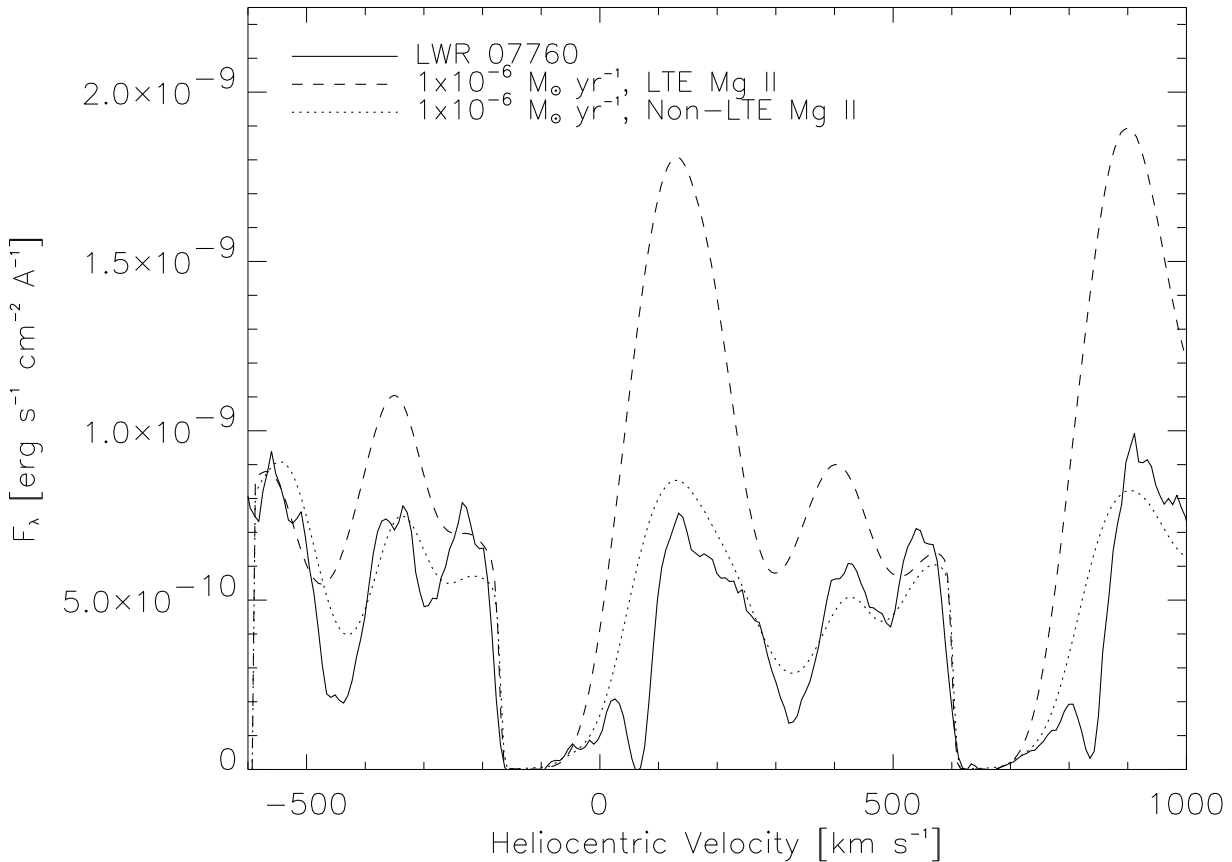
FIG. 19.— *IUE* spectrum LWR 07760 in a region showing the Mg II *h* and *k* resonance lines. Shown for comparison are synthetic spectra from two models: LTE Mg II and non-LTE Mg II. With the exception of the non-LTE metal line-blanketing, these models have identical parameters. The zero-point of the velocity scale is the *h* line, $\lambda_{air} = 2795.523$ Å shifted to radial velocity of Deneb, RV $= -4.5$ km s^{-1} (Evans 1967). The interstellar components at $\sim +70$ km s^{-1}, have not been modeled.

km s^{-1} which are inconsistant with the blue edges of the Mg II h & k profiles (see Figure 19). In the latter work, the critical assumption of a fully ionized wind is made in addition to the assumption of LTE and the Sobolev approximation. As shown above (§5.3, Figure 11), a fully ionized wind is inconsistent with the observed slope of the millimeter-radio continuum.

We have attempted to fit the Hα profile from the HEROS red spectrum by fixing v_∞ at 225 km s^{-1} and computing the synthetic profiles in the co-moving frame from the set of radiative equilibrium expanding atmosphere models computed for the SED analysis. We are unable to improve upon earlier attempts to fit the observed Hα profile by adjusting *any* of the model parameters (see Figure 20). The most significant and persistent discrepancy between the synthetic and observed profiles is the depth of the absorption component, which is significantly weaker in the observed spectrum (residual intensity $\simeq 0.6$). Observed Hα profiles from 1991 (Kaufer et al. 1996) have a broader absorption component than shown in Figure 20, but they are not deeper. Furthermore, while the velocity of absorption component minimum is quite variable, it is rarely, if ever, shifted blueward of –50 km s^{-1}, ~20% of the terminal velocity. Models with mass-loss rates $\dot{M} > 10^{-7}$ M$_\odot$ yr^{-1} produce synthetic profiles with absorption minima shifted to –80 km s^{-1} and beyond. Another problem is that in this same mass-loss range the synthetic profiles show the broad electron scattering wings prominent in other hot supergiants, but lacking in Deneb. Since we are unable to achieve a reasonable fit to the observed Hα profile, it is near impossible to reliably estimate a mass-loss rate from this line. The position of the absorption component relative to the models (Figure 20a) suggests a mass-loss rate in the range: 5×10^{-7} M$_\odot$ yr^{-1} > $\dot{M}$ > 10^{-7} M$_\odot$ yr^{-1}.

Higher members of the Balmer series (Hβ, Hγ, Hδ) are a better match to our synthetic profiles than Hα (see Figure 21). The depth of the observed line cores are well matched by our wind model synthetic profiles which have weaker cores than hydrostatic model synthetic profiles. However, for these same lines the wings are generally fit better by the hydrostatic profiles. The wind profiles also fail to match the weak metal lines in the wings of Hβ and Hγ. In the wind models the column density through the wind is clearly too large and metal lines which should form deeper in the atmosphere are washed out by the velocity field. The data do show the presence of a wind in the Hβ and Brγ lines. The Hβ line core
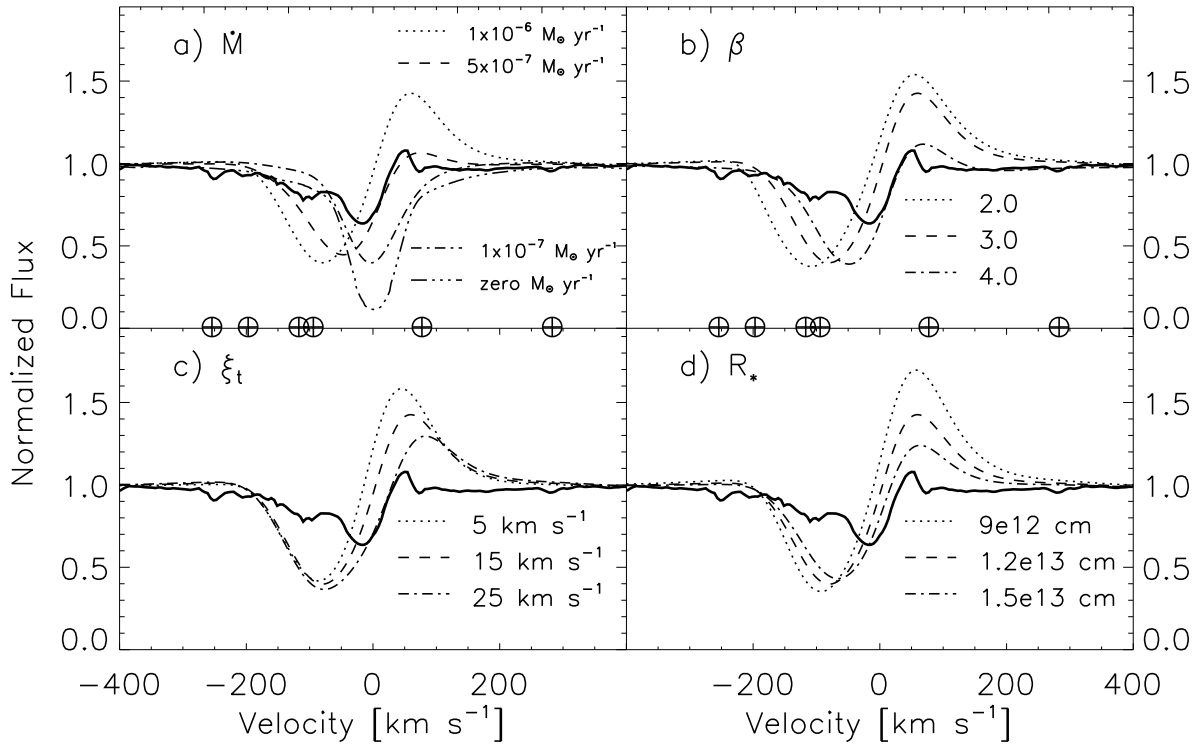

FIG. 20.— HEROS red spectrum (thick solid line) at the Hα line shown with synthetic profiles from a grid of model atmospheres with different parameterizations about the base model ($T_\star = 9000$ K , $\log g(R_\star) = 1.3$, $\dot{M} = 10^{-6}$ M$_\odot$ yr^{-1}, $\beta = 3.0$, $\xi_t = 15$ km s^{-1}). The synthetic profile for zero mass-loss is from the hydrostatic model $T_\star = 8500$ K , $\log g(R_\star) = 1.3$, $\xi_t = 15$ km s^{-1}. Shown are the effects on the synthetic profile due to the (a) mass-loss rate, (b) velocity-law exponent, (c) microturbulence parameter, and (d) the input radius. Positions of telluric lines are mark by $\oplus$ symbols. All synthetic profiles have been shifted from vacuum to air wavelengths and rotationally broadened for $v \sin i = 25$ km s^{-1}.

is shifted slightly blueward from zero velocity and the Brγ profile (see Figure 21d) is noticeably asymmetric in the red wing, suggesting a very weak P-Cygni emission component to this line.

For still higher members of the Balmer series, 2→17 to 2→30, the observed lines are closely matched by the wind model synthetic profiles (see Figure 22a). The hydrostatic model line cores are again too strong. For high members of the Paschen series, 3→15 to 3→22, the difference between the wind and hydrostatic synthetic profiles is less distinct and both predict profiles which are a bit too strong (see Figure 22b). For the last few members of the Pfund series, 5→ 22 to roughly 5→26, the wind and hydrostatic synthetic profiles are nearly indentical and are much stronger than the observed profiles (see Figure 22c). It is expected that for progressively weaker hydrogen series the differences between the wind and hydrostatic models should disappear since these weak lines form deep in the photosphere. It also appears clear that the $n = 5$ level of hydrogen in the models is overpopulated relative to Deneb's photosphere.

The last set of line profiles we show are those from Ca II: the H & K lines and two members of the infrared triplet (IRT) (see Figure 23). The most striking characteristic of the synthetic profiles for the H, K, and $\lambda8542$ lines is the importance of non-LTE. In LTE, Ca^+ is the dominant stage of Ca in the wind and the strong synthetic P-Cygni profiles of the H & K are evidence for this. In the non-LTE models, and apparently in Deneb's expanding atmosphere, most of the Ca is in the form of Ca^{++}, which has its first excited level 25 eV above the ground state, with no strong lines. For the H & K lines, the hydrostatic model synthetic profiles are a bit too strong and the non-LTE wind profiles are a bit too weak. For the model with $\dot{M} = 10^{-6}$ $M_\odot$ yr^{-1}, the synthetic profiles are also significantly blueshifted, suggesting $\dot{M} < 10^{-7}$ $M_\odot$ yr^{-1}. For the two IRT lines, only the stronger $\lambda8542$ line shows a significant departure from LTE. The non-LTE wind model lines are a bit too strong and the hydrostatic profiles are stronger still.

7. SUMMARY AND CONCLUSIONS

A stellar wind module has been developed for the PHOENIX stellar atmosphere code for the purpose of computing atmospheric structures and detailed synthetic spectra of hot luminous stars. These models incorporate a solution of the expanding spherically symmetric radiative transfer equation in the co-moving frame, a treatment of detailed metal
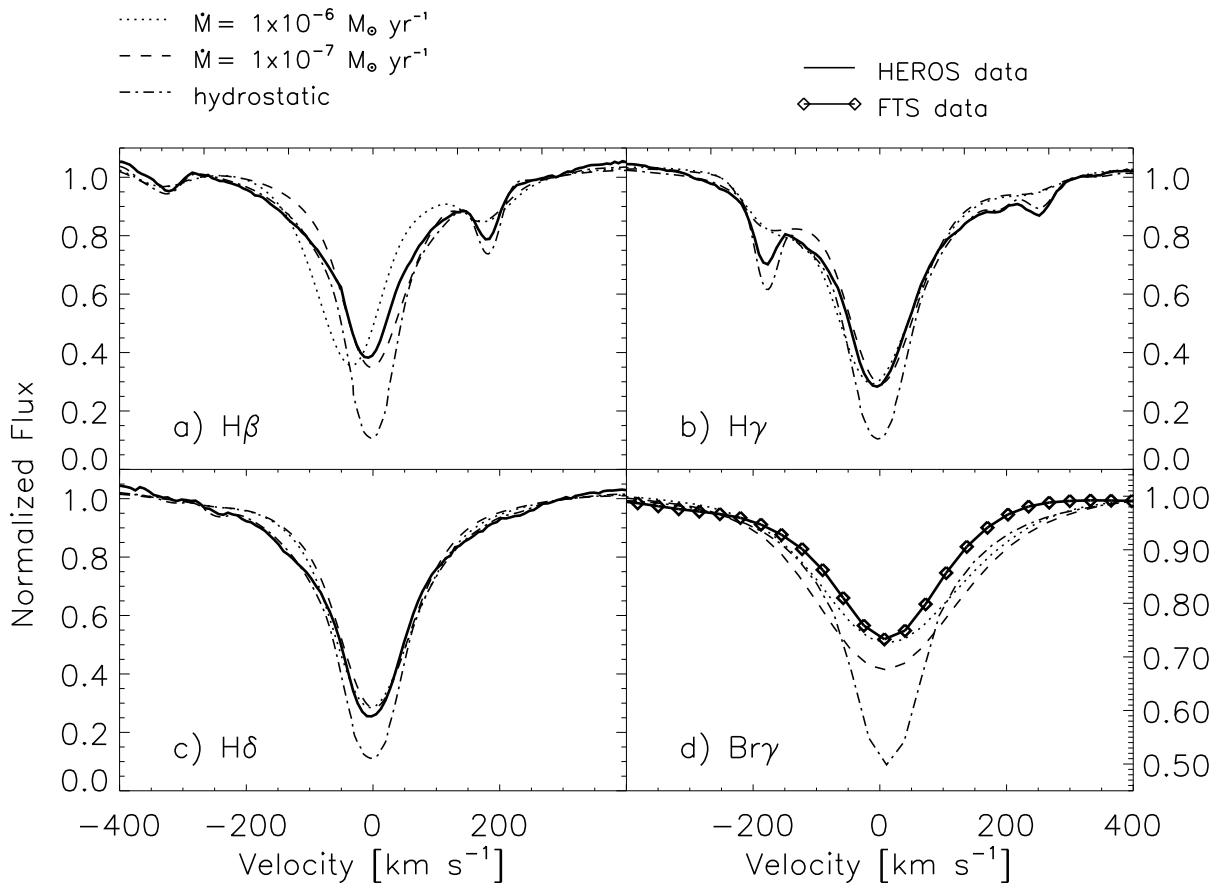

FIG. 21.— HEROS blue spectrum (thick solid line) at (a) Hβ, (b) Hγ, (c) Hδ, and the FTS spectrum (thick solid line with diamonds) at (d) Brγ. Shown for comparison are synthetic profiles from three model atmospheres: two wind models, $T_\star = 9000$ K, $\log g(R_\star) = 1.3$, $\beta = 3.0$, $\xi_t = 15$ km s^{-1}, $\dot{M} = 10^{-6}$ $M_\odot$ yr^{-1} (dotted line) and $\dot{M} = 10^{-7}$ $M_\odot$ yr^{-1}(dashed line), and the hydrostatic model (dash-dot line) $T_\star = 8500$ K , $\log g(R_\star) = 1.3$, $\xi_t = 15$ km s^{-1}. The synthetic profiles for comparison with the HEROS data have been shifted from vacuum to air wavelengths. All synthetic profiles have been rotationally broadened for $v \sin i = 25$ km s^{-1}.
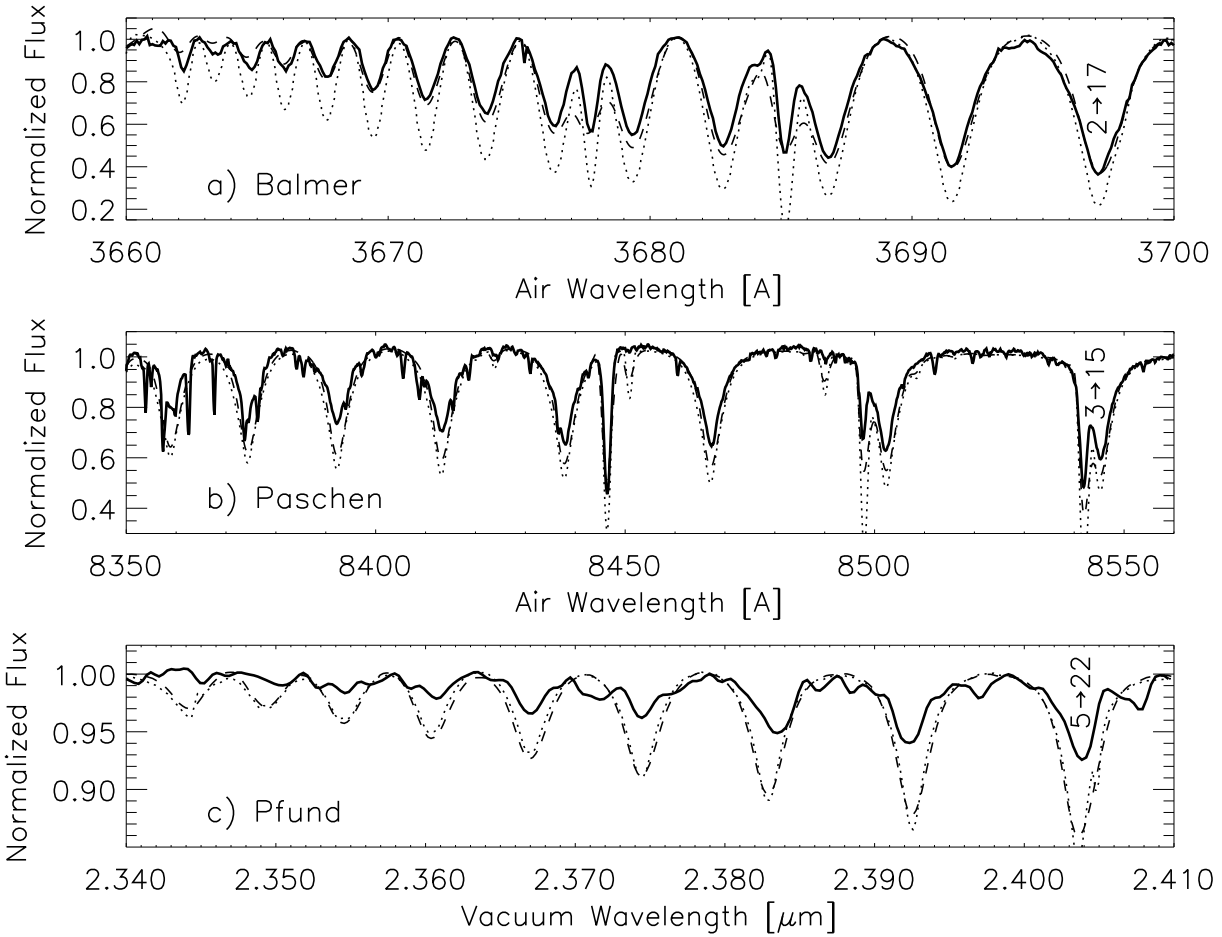
FIG. 22.— Observed hydrogen lines (thick solid lines), from three series: (a) Balmer, (b) Paschen, and (c) Pfund. These lines are all high members of there respective series: (a) 2→17 to 2→30, (b) 3→15 to 3→22, and (c) 5→22 to ∼5→26. Other strong features in the spectra include Cr II λ3678, Ti II λ3685, O I λ8446, and Ca II λλ8498,8542. The Paschen series is contaminated by many weak telluric features. The observed Balmer and Paschen series are from the HEROS blue and red spectra respectively and the Pfund series is from the FTS spectrum. Shown for comparison are synthetic profiles from two model atmospheres: a wind model (dashed line), $T_\star = 9000$ K, $\log g(R_\star) = 1.3$, $\beta = 3.0$, $\xi_t = 15$ km s^{-1}, $\dot{M} = 10^{-6}$ M$_\odot$ yr^{-1} and a hydrostatic model (dotted line) $T_\star = 8500$ K , $\log g(R_\star) = 1.3$, $\xi_t = 15$ km s^{-1}. The synthetic profiles for comparison with the HEROS data have been shifted from vacuum to air wavelengths. All synthetic profiles have been rotationally broadened for $v \sin i = 25$ km s^{-1}.
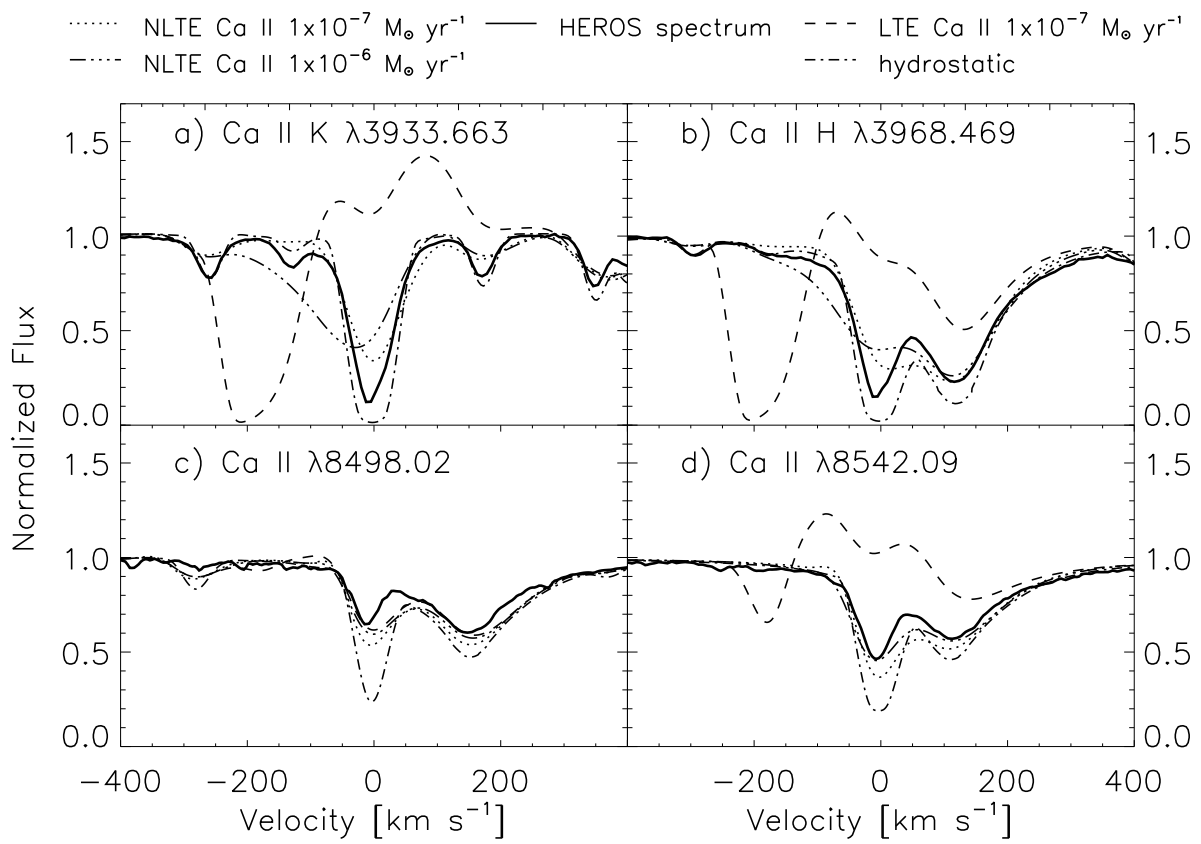
FIG. 23.— HEROS spectra (thick solid lines) at the Ca II lines (a) K, (b) H, (c) $\lambda8498$, and (d) $\lambda8542$. Shown for comparison are synthetic profiles from four model atmospheres: two wind models with non-LTE Ca I-III, plus one wind model and one hydrostatic model with LTE Ca I-III. The wind models: $T_\star = 9000$ K, $\log g(R_\star) = 1.3$, $\beta = 3.0$, $\xi_t = 15$ km s^{-1}, $\dot{M} = 10^{-6}$ M$_\odot$ yr^{-1} (long dash-dot line) and $\dot{M} = 10^{-7}$ M$_\odot$ yr^{-1} (LTE dashed line, non-LTE dotted line) and the hydrostatic model: $T_\star = 8500$ K , $\log g(R_\star) = 1.3$, $\xi_t = 15$ km s^{-1} (short dash-dot line). The synthetic profiles have been shifted from vacuum to air wavelengths. All synthetic profiles have been rotationally broadened for $v \sin i = 25$ km s^{-1}.

line-blanketing in non-local thermodynamic equilibrium, and a convergence of the model temperature structure under the constraint of radiative equilibrium. We have used the model atmospheres and synthetic spectra from this code to better illuminate what we do not understand about the spectral energy distribution, the mass-loss rate, and the fundamental stellar parameters of the A-type supergiant Deneb.

7.1. *Millimeter and Centimeter Radiation Detections*

We have reported the first detections of Deneb at millimeter and centimeter wavelengths with the SCUBA and the VLA. These new data, in conjunction with IR photometery from 2 μm to 60 μm, provide a better glimpse at the thermal continuum from Deneb's extended atmosphere. The slope of the radio spectrum implies a stellar wind where hydrogen is partially ionized, a result reproduced by our models. We find that the effects of line-blanketing on the synthetic millimeter and radio continua are significant and must be taken into when analyzing the continua of partially ionized winds.

7.2. *Angular Diameter Measurement and Limb-darkening*

Visibility measurements from the NPOI indicate a uniform-disk angular diameter for Deneb of $\overline{\theta_{\rm UD}} = 2.40 \pm 0.06$ mas. Our models predict that the center-to-limb profile for Deneb in the *I*-band is significantly extended relative to hydrostatic model predictions. We believe this limb profile causes the uniform disk angular diameter to be larger than the angular diameter $\theta_{\rm Ross} = 2.32 \pm 0.06$ mas corresponding to $R_{\rm Ross}$, the radius at the Rosseland mean optical depth $\tau_{\rm Ross} = 2/3$. The result is a correction to the uniform disk diameter which is less than unity, contrary to the limb-darkening correction made in the calculation of the effective temperature for more compact stars. This limb profile prediction will hopefully be testable in the coming years as longer base-line optical/IR interferometers come on-line.

7.3. *Interferometic Effective Temperature*

Considering the uncertainites in the spectrophotometry, the interstellar extinction, and the corrected NPOI angular diameter, we find an inteferometric fundamental effective temperature of $T_{\rm eff}^{\rm Ross} = 8600 \pm 500$ K for Deneb. The biggest uncertainty in the value of the effective temperature is the uncertainty in the color excess, $E(B - V) = 0.09^{+0.04}_{-0.03}$. This effective temperature together with the distance estimates from *Hipparcos* and Deneb's Cyg OB7 association membership, and theoretical evolutionary tracks yield: $R_{\rm Ross} \simeq 180\ R_{\odot}$, $L \simeq 1.6 \pm 0.4 \times 10^4\ L_{\odot}$, $M \sim 20 - 25\ M_{\odot}$, and $\log g \simeq 1.3$.

7.4. *Least-squares Spectrum Analysis*

A least-squares comparison of 55 synthetic spectral energy distributions from 1220 Å to 3.6 cm with the spectral energy distibution of Deneb provide estimates (1σ) for the star's effective temperature and mass-loss rate of: $T_{\rm eff}^{\rm Ross} \simeq 8420 \pm 100$ K and $\dot{M} \simeq 8 \pm 3 \times 10^{-7}\ {\rm M}_{\odot}\ {\rm yr}^{-1}$. The best fitting models to the SED indicate that the color excess toward Deneb is $E(B-V) = 0.06 \pm 0.01$. This effective temperature is consistent with the inteferometric fundamental effective temperature. The smaller 1σ error in the least-squares value of $T_{\rm eff}^{\rm Ross}$ relative to interferometric value reflects the tighter contraint on the color excess from the least-squares fit. However, both values of $T_{\rm eff}^{\rm Ross}$ are subject to systematic errors due to the poorly established interstellar extinction curve toward Deneb.

The least-squares analysis shows that, in addition to the effective temperature and mass-loss rate, the steepness of β-law velocity field, the microturbulence, and the surface gravity all have a significant effect on the model temperature structure and ultraviolet spectral energy distribution. It is interesting to point out that models with β outside the range 3.0 ± 1.0 provide very poor fits to the UV spectrophotometry and that β values near 3.0 are not consistent with the radiation driven wind models of Achmad et al. (1997), which predict $\beta < 1$ for A-type supergiant winds.

7.5. *Non-LTE Effects on the Line Spectrum*

The mass-loss rate range derived from the least-squares analysis is reasonably consistent with that derived from high dispersion spectra of Deneb when non-LTE metal-line blanketing is treated, in particular for species Fe I-III, Mg II, and Ca I-III. The primary effect of the non-LTE treatment is to enhance the ionization of these elements in the wind relative to LTE. The non-LTE model ionization structure produces much lower column densities of Fe II, Mg II, and Ca II relative to LTE and causes strong lines to form deeper in the wind at lower velocities, in better agreement with the observations. For the Fe II UV lines and the Ca II *H* & *K* lines, the non-LTE effects are striking. The mass-loss rate inferred from the Fe II UV lines is 50 to 100 times larger in non-LTE than in LTE. The synthetic *H* & *K* profiles show strong synthetic P-Cygni profiles in LTE which are not present in the data or in the non-LTE synthetic profiles.

7.6. *Problems with Hα and Other Hydrogen Lines*

We are unable achieve a reasonable fit to a typical Hα P-Cygni profile for Deneb with any model parameters over a reasonable range. The most prominent problem is that the model absorption component is always too strong. While Deneb's Hα profile is variable, it is not hugely variable, and the model Hα profiles don't look like the observed profile at anytime. The wind model line profiles generally provide a better match to the higher Balmer series lines than hydrostatic model line profiles. Both wind models and hydrostatic models match the higher Paschen series lines equally well. Both types of models fail badly for the higher Pfund series lines. These failures indicate that a spherically symmetric, expanding, steady state, line-blanketed, radiative equilibrium structure is not consistent with the conditions under which a typical

Hα and the higher Pfund lines form. The strong lines of Fe II, Mg II, and Ca II that we can reproduce with our models originate from the ground state or low-exitation levels and apparently are not sensitive to the conditions which affect the 2$\rightarrow$3 transition of hydrogen. Our inability to fit a typical Hα profile from Deneb is very bothersome because Hα is the most commonly used mass-loss rate diagnositic for A-type supergiants.

7.7. *Mass-loss Rate*

The thermal millimeter and radio continua of Deneb when compared with our models provide both lower and upper limits to its mass-loss rate. The detection of radiation at 3.6 cm, far in excess of what is expected for no mass-loss, provides the lower limit at about 10^{-7} M$_\odot$ yr^{-1}. The 3σ upper limit to the 870 μm flux provides the upper limit at about 10^{-6} M$_\odot$ yr^{-1}. If Deneb's extended atmosphere departs significantly from spherical symmetry, this would systematically bias our estimates for the mass-loss rate. However, there is no evidence for deviations from spherical symmetry from instrinsic polarization studies, either in the continuum or in the spectral lines Hβ, Hγ, Ca II H (Clarke & Brooks 1984, and references therein).

The line spectrum of Deneb provides mainly upper limits to the mass-loss rate. While the observed P-Cygni character of the Hα and Mg II h and k lines are clear indicators of the stellar outflow, a hydrostatic model with no mass loss is really not that bad a fit to most of the UV line spectrum. It is the more subtle characteristics of the UV lines, their widths and desaturated profiles which show evidence of the velocity field. Many weak metal lines in the optical spectrum are also very well matched by models with no mass-loss and all our models with $\dot{M} > 10^{-8}$ M$_\odot$ yr^{-1} predict profiles for these lines which on average tend to be washed out and too shallow. Certainly the column densities in many of these transitions are too high. While non-LTE ionization effects solve this problem for some lines, others are still problematic. A line-by-line study with a complete grid of models which include Ti I-III, Cr I-III, and other metals in non-LTE is needed to analyze this issue fully. We have model atoms for these species and will investigate this in future work.

While previously published estimates for Deneb's mass-loss rate range over more than three orders of magnitude, we can with confidence reduce this uncertainty to one order of magnitude, but not much better. Reducing this uncertainty further requires a better match simultaneously to the spectral energy distribution and the spectral lines. This may require removing several of our simplifying assumptions such as radial symmetry, homogeniety (filling-factor equal to unity), time-independence, and no mechanical dissipation.

We suggest that before the Wind Momentum-Luminosity Relationship, thus far based solely on Balmer line fits, can be firmly established for A-type supergiants, researchers should work to toward firmly establishing fundamental parameters and stellar wind properties of Galactic A-type supergiants by checking that models are consistant with both the spectral energy distributions and the line spectra.

APPENDIX

A. CONSTRUCTION OF MODEL ATMOSPHERES

The stellar wind module developed by Aufdenberg (2000) for the `PHOENIX` code links a unified model atmosphere structure to the non-LTE line-blanketing and expanding atmosphere radiative transfer modules already in the code. Important improvements over previous models lie in the solution of the radiative transfer equation, the degree of consistent LTE and non-LTE metal line-blanketing, and the solution of the temperature structure from the condition of energy conservation.

A.1. *Line-blanketing Specifics and Non-LTE Model Atoms*

All models presented in this paper include in LTE approximately 7×10^5 of the most important blanketing lines dynamically selected from a list of 42×10^6 lines (Kurucz & Bell 1995) from 39 elements with up to 26 ionization stages in addition to the strongest 517 lines for the spectra H I, He I, He II, which are treated in non-LTE. More sophisticated models include an additional 2.3×10^4 lines in non-LTE for these spectra: C I, C II, C III, N I, N II, N III, O I, O II,O III, Mg I,Mg II,Mg III, Ca I, Ca II, Ca III, Fe I, Fe II, Fe III. The number of levels and lines from each species are shown in Table A8. For the complete set of non-LTE model ions in the PHOENIX code see Short et al. (1999). The references to the atomic data used to construct the model atoms and ions are given in Table A9.

The non-LTE lines from the model atoms and ions replace the LTE lines and all the lines that are not in non-LTE are handled in LTE as an approximation. Details on non-LTE blanketing techniques can be found in (Short et al. 1999, and references therein). Even in our most sophisticated models the vast majority of lines are treated in LTE. The bulk of the *total opacity* is, however, computed in detailed non-LTE. The line-blanketing is *true* line-blanketing in the sense that the effect of these millions of lines on the temperature structure is computed through the condition of radiative equilibrium (see below). Therefore, the line-blanketing is consistently included in both the model atmosphere and final synthetic spectrum calculations.

A.2. *The Wind Module*

We treat the problem of radiation-driven winds with the following simplifying assumptions: (1) time-independent, steady-state; (2) no magnetic fields or rotation; (3) radial symmetry; and (4) a smooth single-phase flow with no mechanical dissipation, heat conduction, viscosity, or advection.

A.2.1. *Atmospheric Structure and Boundary Conditions*

The gas escaping from the model star is treated as a hydrodynamic flow, satisfying the conservation of mass, momentum, and energy. The mass conservation is specified by the equation of continuity,

$$\dot{M} = 4\pi r^2 \rho(r) v(r) \tag{A1}$$

where $\dot{M}$ is the steady state mass-loss rate, $\rho(r)$ is the gas density, and $v(r)$ is the velocity field. The velocity field is specified by a β-law of the form

$$v(r) = v_\infty (1 - R_\star/r)^\beta. \tag{A2}$$

The layers of the atmosphere below $R_\star$ are modeled as hydrostatic and in these layers the velocity is set to zero.

The structure of the outer wind layers is computed on a fixed radial grid. The structure of the inner hydrostatic layers of the atmosphere is computed on an optical depth grid. Typically 50 layers are used consisting of 35 layers for the wind region and 15 layers for the hydrostatic region. The radial grid points are prescribed by a power-law in order to finely sample the inner region of the wind (Steffen et al. 1997), where the velocity gradient is steepest, and to coarsely sample the outer portion of the wind where the velocity gradient is small.

Table A8

Number of Levels and Primary Transitions[a] Treated in Non-LTE

Element	Stage of Ionization		
	I	II	III
H	30/435	...	...
He	19/37	10/45	...
C	228/1387	85/336	79/365
N	252/2313	152/1110	87/226
O	36/66	171/1304	137/765
Mg	273/835	72/340	91/656
Ca	194/1029	87/455	150/1661
Fe[b]	494/6903	617/13675	566/9721

[a]Primary transitions are those that connect observed levels and have $\log(gf)$ values greater than -3.

[b]Values for the complete models of stages I-III of Fe are shown. In our calculations, only the first 200 levels of each stage are used.

A.2.2. *Wind region*

The radii $r(l)$ in layers $l = 1, ..., l_\star$ are specified by,

$$r(l) = r(1) + \left\{r(l_\star) - r(1)\right\} \cdot \left\{\frac{\alpha^{(l-1)} - 1}{\alpha^{(l_\star-1)} - 1}\right\} \tag{A3}$$

where $l_\star$ is the layer (typically layer 35) immediately above the dynamic-static transition. Layer 1 is the outermost layer and typically we choose the radial extension in the wind to be a factor of 200, $r(1) = 200R_\star$. The value of $r(l_\star)$ is iteratively selected to provide a predetermined degree of smoothness in the density profile across the dynamic-static transition. Generally the jump in density must be less than a factor of 5 across the transition. The input parameter α may be adjusted to optimize the distribution of radial points for a specific velocity field (typically, $\alpha \simeq 1.5$).

The density $\rho(r)$ in the expanding layers is specified from the mass flux continuity equation (A1), where the velocity field has the form of a β-law from equation (A2). The input radius $R_\star$ and the model effective temperature $T_\star$ set the luminosity L of the star,

$$L = 4\pi R_\star^2 \sigma T_\star^4. \tag{A4}$$

Since we use a form of the β-law lacking a macroturbulent velocity, the switch in the structure setup from the dynamic layers to the static layers occurs near the point in the atmosphere where the wind velocity, $v(r)$, drops below the microturbulent velocity, ξ_t. An initial guess at this radius, $r(l_\star) \gtrsim R_\star$, is calculated by finding the radius at which $v(r) = \xi_t$ from equation (A2):

$$r(l_\star) = \frac{R_\star}{\left\{1 - \left(\xi_t/v_\infty\right)^{1/\beta}\right\}}. \tag{A5}$$

This radius is then adjusted inward slightly to improve the degree of smoothness of the density profile across the dynamic-static transition. In practice, this results in a discontinuity in the velocity field across dynamic-static boundary which is very small ($\sim$0.2 km s^{-1}), much smaller than the microturbulent width of the lines, $\xi_t \geq 5$ km s^{-1}.

A.2.3. *Hydrostatic region*

In the hydrostatic layers ($l = l_\star + 1, ..., N$), the structure is computed on a fixed logarithmically spaced optical depth grid,

$$\log\{\tau(l)\} = \log\{\tau(l_\star)\} + (l - l_\star)\left\{\frac{\log\{\tau(N)\} - \log\{\tau(l_\star)\}}{N - l_\star}\right\} \tag{A6}$$

The inner continuum extinction optical depth boundary, $\tau(N) = \tau(2000\text{Å}) = 10^2$, is set well below the thermalization depth. The pressure structure is computed by numerically integrating the hydrostatic equation,

$$\frac{dP}{d\tau} = \frac{g_{\text{eff}}}{\kappa} \tag{A7}$$

TABLE A9
ATOMIC DATA SOURCES FOR MODEL ATOMS AND IONS[a]

Model Species	Levels	$b - b$ cross-sections		$b - f$ cross-sections	
		Radiative	Collisional[b]	Photoionization[c]	Collisional
H I	Johnson	Johnson	Johnson	M84	Drawin
He I	Martin	WSG	BK, Lanzafame	M84	MS
He II	Johnson	Johnson	Johnson	M84	MS
C I-III	KB	KB	Allen, VR	BRP, RM	Drawin
N I-III	KB	KB	Allen, VR	BRP, RM	Darwin
O I	KB	KB	Allen, VR	BRP, RM	CLL
O II-III	KB	KB	Allen, VR	BRP, RM	Drawin
Mg I-III	KB	KB	Allen, VR	RM	Drawin
Ca I-III	KB	KB	Allen, VR	BRP, RM	Drawin
Fe I-III	KB	KB	Allen, VR	BRP, RM	Drawin

[a]References - Allen = Allen (1973); BK = Berrington & Kingston (1987); BRP = Bautista et al. (1998); KB = Kurucz & Bell (1995); CLL=Chung et al. (1993, 1994); Drawin = Drawin (1961); Lanzafame = Lanzafame et al. (1993); M84 = Mathisen (1984); MS = Mihalas & Stone (1968); Johnson = Johnson (1972); RM = Reilman & Manson (1979); VR = Van Regemorter (1962); WSG = Wiese et al. (1966)

[b]Reference to Allen is only for cross-sections between bound levels not coupled by radiative transitions

[c]Reference to BRP is only for ground-state cross-sections

where g_{eff} is the effective gravitational acceleration

$$g_{\mathrm{eff}} = g(R_\star)\frac{R_\star^2}{r^2} - g_{\mathrm{rad}}(r) \tag{A8}$$

the difference of the Newtonian acceleration and the radiative acceleration g_{rad} computed from

$$g_{\mathrm{rad}}(r) = \frac{1}{c\rho(r)}4\pi \int_0^\infty \chi_\lambda(r)H_\lambda(r)\,d\lambda, \tag{A9}$$

where $\chi_\lambda(r)H_\lambda(r)$ is the product of the total line and continuum opacity with the first moment of the radiation field provided by solution of the radiative transfer equation (see below).

The radii in the hydrostatic layers are computed by integrating

$$dr = \frac{1}{\kappa\rho}\,d\tau. \tag{A10}$$

Once the velocity field and radii are computed for all layers, the non-grey, non-LTE radiative transfer problem is solved and the temperature structure is adjusted iteratively to achieve energy conservation.

A.3. *Radiative Transfer and Radiative Equilibrium*

The spherically symmetric radiative transfer equation (SSRTE) in the co-moving (Lagrangian) frame (Mihalas & Weibel-Mihalas 1984)

$$\begin{aligned}
\gamma(\mu+\beta)\frac{\partial I}{\partial r} \quad &+ \frac{\partial}{\partial\mu}\left\{\gamma(1-\mu^2)\left[\frac{(1+\beta\mu)}{r} - \gamma^2(\mu+\beta)\frac{\partial\beta}{\partial r}\right]I\right\} \\
&- \frac{\partial}{\partial\lambda}\left\{\gamma\left[\frac{\beta(1-\mu^2)}{r} + \gamma^2\mu(\mu+\beta)\frac{\partial\beta}{\partial r}\right]\lambda I\right\} \\
&+ \gamma\left\{\frac{2\mu+\beta(3-\mu^2)}{r} + \gamma^2(1+\mu^2+2\beta\mu)\frac{\partial\beta}{\partial r}\right\}I \\
&= \eta - \chi I.
\end{aligned} \tag{A11}$$

is solved using an Operator Splitting/Approximate Λ-operator Iteration (OS/ALI) method using short-characteristics (Hauschildt 1992a). Improvements since this work include a more accurate discretization of the $\partial(\lambda I)/\partial\lambda$ term needed to improve the numerical accuracy necessary for β-law winds.

In equation (A11), μ is the direction-cosine, I is the specific intensity, the velocity is measured in units of the speed of light c, $\beta(r) = v(r)/c$, and $\gamma = 1/(1-\beta^2)^{1/2}$. The principal reason for choosing to solve the radiative transfer problem in the co-moving, fluid rest frame is that although the frequency spectrum may be complex, with many overlapping lines, the opacity is isotropic. This leads to great simplification in the radiation-matter interaction terms relative to the observer's frame equation. For example, the flow velocity is not an argument of the line profile function in the co-moving frame. Frequencies are measured in the frame of the moving fluid, therefore we can use a static line profile. In this frame one can directly integrate over angle and use co-moving-frame moments of the radiation field in the computation of the radiation pressure and radiative equilibrium equations. The angular dependence of the opacity in the observer's frame leads to computational difficulties, and in flows with small velocity gradients and many overlapping spectral lines, escape probability methods, like the Sobolev approximation, are not valid.

We iteratively compute the temperature structure from the condition of energy conservation in the co-moving frame. The conservation of energy, assuming radiative equilibrium, can be specified in the Lagrangian frame (Hauschildt 1992b) by

$$\int_0^\infty (\eta_\lambda - \chi_\lambda J_\lambda)\,d\lambda + \dot{S} = 0 \tag{A12}$$

where η_λ and J_λ describe the emissivity and mean intensity respectively. We include the kinetic and gravitational energy of the wind, $\dot{S}$, in the energy equation, although they are less than 0.1% of the total nuclear energy generated by the star for the models presented here and thus have negligible effect on the temperature structure. For very high wind momenta and small luminosities, the energy required to drive the wind might be large enough to affect the temperature structure. Our numerical solution of the special relativistic radiative energy equation is described in Hauschildt & Baron (1999).

Energy conservation errors are typically $< 1\%$ in both the luminosity and luminosity derivative in each layer. Models are started from a grey temperature structure and iterations are performed with continuum opacity only. Next, more iterations are performed with the addition of full LTE metal-line blanketing opacity. This yields a converged LTE line-blanketed model. Non-LTE models are converged starting from converged LTE line-blanketed models. Non-LTE species are added and the model structure is converged in a series of steps: first H and He; next C, N, O; next Mg, Ca, Fe, etc.

REFERENCES

Abbott, D. C., Telesco, C. M., & Wolff, S. C. 1984, ApJ, 279, 225

Achmad, L., Lamers, H., & Pasquini, L. 1997, A&A, 320, 196

Albayrak, B. 2000, A&A, 364, 237

Allen, C. W. 1973, Astrophysical quantities (London: University of London, Athlone Press, —c1973, 3rd ed.)

Aufdenberg, J. P. 2000, PhD thesis, Arizona State University

Aufdenberg, J. P., Hauschildt, P. H., & Baron, E. 1999, MNRAS, 302, 599

Baars, J. W. M., Martin, R. N., Mangum, J. G., McMullin, J. P., & Peters, W. L. 1999, PASP, 111, 627

Barlow, M. J. & Cohen, M. 1977, ApJ, 213, 737

Barnes, T. G., Evans, D. S., & Moffett, T. J. 1978, MNRAS, 183, 285

Barnes, T. G., Evans, D. S., & Parsons, S. B. 1976, MNRAS, 174, 503

Baschek, B., Scholz, M., & Wehrse, R. 1991, A&A, 246, 374

Bautista, M. A., Romano, P., & Pradhan, A. K. 1998, ApJS, 118, 259

Berrington, K. A. & Kingston, A. E. 1987, Journal of Physics B Atomic Molecular Physics, 20, 6631

Bessell, M. S. 1990, PASP, 102, 1181

Bevington, P. R. 1969, Data Reduction and Error Analysis for the Physical Sciences (McCraw-Hill)

Bohlin, R. C. & Holm, A. V. 1984, IUE Newsletter, 24, 74

Bonneau, D., Koechlin, L., Oneto, J. L., & Valkili, F. 1981, A&A, 103, 28

Breger, M. 1976, ApJS, 32, 7

Bresolin, F., Kudritzki, R., Mendez, R. H., & Przybilla, N. 2001, ApJ, 548, L159

Cardelli, J. A., Clayton, G. C., & Mathis, J. S. 1989, ApJ, 345, 245

Chung, S., Lin, C. C., & Lee, E. T. P. 1993, Phys. Rev. A, 47, 3867

—. 1994, Journal of Quantitative Spectroscopy and Radiative Transfer, 51, 629

Claret, A. 2000, A&A, 363, 1081

Clarke, D. & Brooks, A. 1984, MNRAS, 211, 737

Code, A. D. & Meade, M. R. 1979, ApJS, 39, 195

Drake, S. A. & Linsky, J. L. 1989, AJ, 98, 1831

Drawin, H. W. 1961, Zs. f. Phys., 164, 513

Edvardsson, B., Andersen, J., Gustafsson, B., Lambert, D. L., Nissen, P. E., & Tomkin, J. 1993, A&A, 275, 101

Egan, M. P., Price, S. D., Moshir, M. M., Cohen, M., Tedescco, E. F., Murdock, T. L., Zweil, A., Burdick, S., Bonito, N., Gugliotti, G. M., & Duszlak, J. 1999, MSX Point Source Catalog Explanatory Guide No. AFRL-VS-TR-1999-1522 (Air Force Research Laboratory)

Evans, D. S. 1967, in IAU Symp. 30: Determination of Radial Velocities and their Applications, Vol. 30, 57

Fitzpatrick, E. L. & Massa, D. 1990, ApJS, 72, 163

Gabriel, C., Acosta-Pulido, J., Heinrichsen, I., Morris, H., & Tai, W. . 1997, in ASP Conf. Ser. 125: Astronomical Data Analysis Software and Systems VI, Vol. 6, 108

Glushneva, I. N., Kharitonov, A. V., Knyazeva, L. N., & Shenavrin, V. I. 1992, A&AS, 92, 1

González-Riestra, R., Cassatella, A., Solano, E., Altamore, A., & Wamsteker, W. 2000, A&AS, 141, 343

Grevesse, N. & Noels, A. 1993, in Origin and Evolution of the Elements, ed. N. Prantos, E. Vangioni-Flam, & M. Casse (Cambridge University Press), p.14

Hauschildt, P. H. 1992a, JQSRT, 47, 433

—. 1992b, ApJ, 398, 224

Hauschildt, P. H. & Baron, E. 1999, J. Comp. and App. Math., 109, 41

Heger, A. & Langer, N. 2000, ApJ, 544, 1016

Henize, K. G., Wray, J. D., Parsons, S. B., & Benedict, G. F. 1979, Catalog of far-ultraviolet objective-prism spectrophotometry: SKYLAB experiment S-019, ultraviolet steller astronomy, Reference Publication 1031, NASA

Hensberge, H., de Loore, C., Lamers, H. J. G. L. M., & Bruhweiler, F. C. 1982, A& A, 106, 137

Hummer, D. G. & Rybicki, G. B. 1971, MNRAS, 152, 1

Humphreys, R. M. 1978, ApJS, 38, 309

Jamar, C., Macau-Hercot, D., Monfils, A., Thompson, G. I., Houziaux, L., & Wilson, R. 1976, in Ultraviolet Bright Star Spectrophotometric Catalogue, ESA Special Report 27

Jenniskens, P. & Greenberg, J. M. 1993, A&A, 274, 439

Johnson, H. L., Iriarte, B., Mitchell, R. I., & Wisniewskj, W. Z. 1966, Communications of the Lunar and Planetary Laboratory, 4, 99

Johnson, L. C. 1972, ApJ, 174, 227+

Kaufer, A. 1999, private communication.

Kaufer, A., Stahl, O., Wolf, B., Gaeng, T., Gummersbach, C. A., Kovacs, J., Mandel, H., & Szeifert, T. 1996, A&A, 305, 887

Koechlin, L. & Rabbia, Y. 1985, A&A, 153, 91

Kudritzki, R. P., Puls, J., Lennon, D. J., Venn, K. A., Reetz, J., McCarthy, J. K., & Herrero, A. 1999, A&A, 350, 970

Kunasz, P. B. & Morrison, N. D. 1982, ApJ, 263, 226

Kunasz, P. B. & Praderie, F. 1981, ApJ, 247, 949

Kurucz, R. L. 1994, Atomic Data for Fe, Co, and Ni, Kurucz CD-ROM No. 22 (Cambridge: SAO)

Kurucz, R. L. & Bell, B. 1995, Atomic Line List, Kurucz CD-ROM No. 23 (Cambridge: SAO)

Lanzafame, A. C., Tully, J. A., Berrington, K. A., Dufton, P. L., Byrne, P. B., & Burgess, A. 1993, MNRAS, 264, 402+

Lemke, D., Klaas, U., Abolins, J., Abraham, P., Acosta-Pulido, J., Bogun, S., Castaneda, H., Cornwall, L., Drury, L., Gabriel, C., Garzon, F., Gemuend, H. P., Groezinger, U., Gruen, E., Haas, M., Hajduk, C., Hall, G., Heinrichsen, I., Herbstmeier, U., Hirth, G., Joseph, R., Kinkel, U., Kirches, S., Koempe, C., Kraetschmer, W., Kreysa, E., Krueger, H., Kunkel, M., Laureijs, R., Luetzow-Wentzky, P., Mattila, K., Mueller, T., Pacher, T., Pelz, G., Popow, E., Rasmussen, I., Rodriguez Espinosa, J., Richards, P., Russell, S., Schnopper, H., Schubert, J., Schulz, B., Telesco, C., Tilgner, C., Tuffs, R., Voelk, H., Walker, H., Wells, M., & Wolf, J. 1996, A&A, 315, L64

Mathisen, R. 1984, Photo Cross-sections for Stellar Atmosphere Calculations — Compilation of References and Data, Inst. of Theoret. Astrophys. Univ. of Oslo, Publ. Series No. 1.

McCarthy, J. K., Kudritzki, R. P., Lennon, D. J., Venn, K. A., & Puls, J. 1997, ApJ, 482, 757

Meade, M. R. 2001, private communication

Mihalas, D., Kunasz, P. B., & Hummer, D. G. 1975, ApJ, 202, 465

Mihalas, D. & Stone, M. E. 1968, ApJ, 151, 293+

Mihalas, D. & Weibel-Mihalas, B. 1984, Foundations of Radiation Hydrodynamics (Oxford: Oxford University Press)

Morgan, W. W. & Keenan, P. C. 1973, ARA&A, 11, 29

Neckel, T., Klare, G., & Sarcander, M. 1980, A&AS, 42, 251

Nordgren, T. E., Germain, M. E., Benson, J. A., Mozurkewich, D., Sudol, J. J., Elias, N. M., Hajian, A. R., White, N. M., Hutter, D. J., Johnston, K. J., Gauss, F. S., Armstrong, J. T., Pauls, T. A., & Rickard, L. J. 1999, AJ, 118, 3032

Perryman, M. A. C., Lindegren, L., Kovalevsky, J., Hoeg, E., Bastian, U., Bernacca, P. L., Crézé, M., Donati, F., Grenon, M., van Leeuwen, F., van Der Marel, H., Mignard, F., Murray, C. A., Le Poole, R. S., Schrijver, H., Turon, C., Arenou, F., Froeschlé, M., & Petersen, C. S. 1997, A&A, 323, L49

Praderie, F., Talavera, A., & Lamers, H. J. G. L. M. 1980, A&A, 86, 271

Price, S. D., Egan, M. P., Carey, S. J. G., Mizuno, D., & Kuchar, T. A. 2001, AJ, in press

Quirrenbach, A., Mozurkewich, D., Buscher, D. F., Hummel, C. A., & Armstrong, J. T. 1996, A&A, 312, 160

Reilman, R. F. & Manson, S. T. 1979, ApJS, 40, 815

Rodríguez-Pascual, P. M., González-Riestra, R., Schartel, N., & Wamsteker, W. 1999, A&AS, 139, 183

Rosendhal, J. D. 1972, ApJ, 178, 707

Santolaya-Rey, A. E., Puls, J., & Herrero, A. 1997, A&A, 323, 488

Schaller, G., Schaerer, D., Meynet, G., & Maeder, A. 1992, A&AS, 96, 269

Schulz, B., Huth, S., Kinkel, U., Lemke, D., Acosta-Pulido, J. A., Braun, M., Cast, Cornwall, L., Gabriel, C., Heinrichsen, I., Herbstmeier, U., Klaas, U., Laureijs, R. J., & Muller, T. G. 1999, ESA SP-427: The Universe as Seen by ISO, 427, 965

Scuderi, S., Bonanno, G., Di Benedetto, R., Spadaro, D., & Panagia, N. 1992, ApJ, 392, 201

Scuderi, S., Panagia, N., Stanghellini, C., Trigilio, C., & Umana, G. 1998, A& A, 332, 251

Short, C. I., Hauschildt, P. H., & Baron, E. 1999, ApJ, 525, 375

Simon, M., Felli, M., Cassar, L., Fischer, J., & Massi, M. 1983, ApJ, 266, 623

Steffen, M., Szczerba, R., Men'Shchikov, A., & Schoenberner, D. 1997, A&AS, 126, 39

Takeda, Y. 1994, PASJ, 46, 181

Van Regemorter, H. 1962, ApJ, 136, 906

Venn, K. A. 1995a, ApJS, 99, 659

—. 1995b, ApJ, 449, 839

Verdugo, E., Talavera, A., & Gómez De Castro, A. I. 1999, A&A, 346, 819

Wallace, L. & Hinkle, K. 1997, ApJS, 111, 445

Weaver, W. B. & Torres-Dodgen, A. V. 1995, ApJ, 446, 300

Welty, D. E., Hobbs, L. M., & Kulkarni, V. P. 1994, ApJ, 436, 152

Wiese, W. L., Smith, M. W., & Glennon, B. M. 1966, Atomic Transition Probablities – Hydrogen Through Neon, Tech. Rep. NSRDS-NBS 4, National Bureau of Standards